Scent of Science

Model Creation for Odour Based Control of Robotic Vehicles

Final Report

Authors: Christopher Nicol[1], Dr. A Alex Ellery[1], Dr. Ed Cloutis[2], Brian Lynch[1], Luke O'Connor[3], Dr. Guido de Croon[3]
Affiliations: [1]Carleton University, [2]University of Winnipeg, [3]ESA ACT

Date: 27 July 2013

Contacts:

Lauralee Raffelsieper
Tel: (1) 613-520-2600 ext. 1126
Fax: (1) 613-520-3945
e-mail: lauralee_raffelsieper@carleton.ca

Leopold Summerer (Technical Officer)
Tel: +31(0)715654192
Fax: +31(0)715658018
e-mail: act@esa.int

Ariadna ID: 11-6301
Ariadna study type: Standard
Contract Number: 4000104575/11/NL/KML

Available on the ACT website
http://www.esa.int/act

Introduction

As technology improves, the capacity for our robotic vehicles to do scientific inquiries on other planetary bodies increases. Communication opportunities between these vehicles and their human operators on Earth are not increasing at the same rate, meaning the length of time to receive information from our rovers on other planets is increasing. This leads to longer missions with less area being explored. In order to maximize the amount of traveling the rover can accomplish between commands from the human operator, while still ensuring the rover does not miss any scientific 'interesting' places, scientist and engineers are working on ways for the rover to autonomously make decisions. This first began with autonomous navigation, guidance and control; the human operator would specify a new location for the rover to move and the rover would travel their autonomously deciding on the best path to take to avoid obstacles like rocks and steep hills. This allows for longer travels before a human has to receive data and respond with a new command.

The next phases of autonomy is giving the vehicle a level of decision making with respect to its final destination, where it will conduct scientific experiments relating to the geology, chemistry, and biology of the area. We call this "autonomous science." The challenge with autonomous science is programming the vehicle to judge the scientific value of one site from another from afar. Many animals and insects on Earth use scents to aid them in everyday life; for various functions such as finding food (lobsters), attracting mates (moths), or marking paths back to their hives (ants). Odor detection, as well as algorithms for determining the source(s) of the odor have been used terrestrially for functions like determining where a gas leak is occurring in a building, or the location of a burst pipe in the case of underwater oil pipelines.

There are many space applications where we are looking for a specific target from which a plume of either material or markers is emitted. In this way, we use the analogy of finding an odor source to these related problems. One of the most direct analogies is the detection of methane sources on Mars, in which we would literally be tracking the odor plume to the source. This is made difficult by the low amounts of methane on Mars, as well as the high turbulent diffusion that occurs. It is probable that a vehicle on Mars would detect methane sporadically, and would have very little information to use in finding the source. A more metaphorical example is targeting the water geyser locations on Saturn's moon Enceladus with a decent vehicle. If we were to attempt to land on this moon, the most interesting landing site would be on, or extremely close, to one of the geyser locations. The water particles being ejected into space can be thought of as an 'odor', and the geyser location is the source which we attempt to precisely locate. Some of the many challenges in this situation are the multiple jets which make up Enceladus' plume. Targeting a single source at high speeds may prove to be difficult. If a submarine vehicle were to be deployed into the ocean of Europa, one of its targets would be to search for hydrothermal vents which are thought to exist. Markers emitted from hydrothermal vents include pockets of heat as well as certain chemical compounds.

This report details the work done towards developing a methodology for locating scientifically interesting targets by using the analogy of 'sniffing.' The "Scent for Science" study is intended to build some of the knowledge and tools necessary to develop this methodology further. This study is funded through the Ariadna program and is a partnership between Carleton University and the Advanced Concepts Team at the European Space Agency. Although using the analogy of scent in locating scientific interesting sites is not always practical, we are working to develop it as one of many reliable tools that we can use to assist in both the quantity and quality of scientific information gathered in space exploration missions.

The remainder of the report is outlined as follows. In Chapter 1, an odor spreading model that focuses on Martian methane is introduced. Subsequently, in Chapter 2, a model is developed for the geyser jets on Enceladus. Then, in Chapter 3, two attempts are described to perform odor source localization with neural networks. The first attempt consists of a Kalman filtering approach, while the second attempt uses backpropagation for training recurrent neural networks. Finally, conclusions are drawn in Chapter 4.

Please note that the majority of this report consists of the contributions of the Carleton University team. The contribution of the Advanced Concepts Team mainly consists of helping with debugging and significantly accelerating the methane model code. In addition, the team has separately investigated an evolutionary approach to optimize neural networks for autonomous odor source localization. This approach will briefly be described at the end of Chapter 3.

Chapter 1

Mars Methane

1.1 Introduction

Three individual measurements of atmospheric Martian methane occurred in 2003 and 2004. Formisano et al. (2004) reported detection from on-board Mars Express using the Planetary Fourier Spectrometer. At the same time Krasnopolsky et al. (2004) used the Fourier Transform Spectrometer at the Canada-France-Hawaii Telescope to observe methane. Finally, Mumma et al. (2009) published results of detection during the northern summer of 2003 using a ground based high-dispersion infrared spectrometers. More spectacular than the discovery of methane in the Martian atmosphere is the spatial and temporal variability of concentration. Lefèvre and Forget (2009) note that the seasonal variability of the concentration shown in two of the experiments do not match the expected 300 year lifetime of methane based on known chemistry. Zahnle et al. (2011) further question the results of the observations pointing out that the filtering of Earth's atmosphere out of the ground-based measurements is difficult and can easily produce false results. In order to gather more evidence for, or against the presence of methane on Mars, the Mars Science Laboratory (MSL) mission's Curiosity rover, which is scheduled to land on Mars in early August, will be featuring an advance sensor suite to measure methane concentrations both in the atmosphere and in soil samples (Webster and Mahaffy, 2011).

Confirmation of atmospheric methane by the Curiosity rover would imply either geological or biological activity occurring on Mars. The small time scales of the methane measurements imply that an active source exists and that some sort of destruction process is taking place. Chastain and Chevrier (2007) noted that methane clathrates are a viable source for the methane on Mars. Methane clathrate deposits are expected on Mars, and the dissociation of the gas can occur in many nature processes. Chassefière (2009) further discuss the possibility of metastable clathrates as evidence by the ratio of methane and water vapor. This hypothesis helps to explain the time scale of methane production/losses; the expected lifetime of methane due to clathrate models are 6 months as opposed to earlier atmospheric models which predict 300 years. Martian dust storms have also been suggested to act as a possible methane sink, further reducing its lifetime (Farrell et al., 2006).

The next logical step in determining the source of methane on Mars is to seek out local sources of the measured methane in order to determine its origin. Many diverse robotic plume tracing algorithms have been developed for terrestrial purposes, most for laminar conditions. We expect that any local methane plume on Mars will be turbulent in nature. Terrestrial algorithms tend to use a map,implicitly constraining the robot in its search for the source to the area in its map. Boundary constraints are acceptable for terrestrial applications when it is assumed that some previous information is available about the source being searched for. Planetary exploration missions may not be so nicely constrained due to a lack of prior information about a lot of the regions being searched. Any information about the Martian methane plume will have a resolution of kilometers which does not sufficiently constrain the plume for the previously mentioned methods. Therefore, we work towards an egocentric, reactionary algorithm which does not require a bounded map.

In order to develop and test algorithms for tracking Martian methane we develop a simulation of the fine structure of the methane plume. Many models for long-term averages of atmospheric plumes exist. They are characterized as Gaussian, smooth, and constant. In nature, these characteristics are not observed as integration times for measurements are much shorter time scales than the time needed for a measurement which would be representative of a Gaussian plume. The plumes we wish to model are characterized as patchy, stochastic, and time-variant. Inside the plume are many spaces of 'clean' air whose concentration are undistinguished from background levels. Also unlike the Gaussian plume, the concentration gradient oftentimes do not point in the direction of the source. Lastly the concentration at each location varies with time. We wish to capture all these characteristics in our model.

Despite the requirement of the rover control to be egocentric with no maps, the simulation of the plume can be bounded provided that the simulation area is large enough that the rover does not stray outside the boundaries. This model is based on solving partial differential equations which describe the transfer of methane from a source over time. Validation of the model is important to ensure that the methods we develop for source-localization are effective. Jones (1983) adapted the statistical analysis that Chatwin (1982) used to describe puffs of gas, and used them to describe atmospheric plumes. His experiments allowed him to quantify the properties of a ionized air plume by placing sensors at four discrete locations along the plume centerline. Farrell et al. (2002) use the same statistical scheme and Jones' results to validate their filament-based model of a moth's pheromone plume. We will compare the results of our model along side both of these previous works, albeit we expect slightly different trends for a Martian plume as compared to the atmospheric plume of Jones and the modeled plume of Farrell.

1.1.1 Article Overview

The next section reviews the statistical methods and terms previous authors have used to characterize both experimental data and odor models. Next, comparison of conditions which would affect plume structure on Earth and Mars is presented. This leads to the formulation of desired characteristics for the plume model, and the estimate of properties of the statistical analysis which would validate the model. The model is then presented in its entirety: the defining equations of state, the source reactions, the advection and turbulent diffusion models. Limitations placed on the model due to computation and the numerical solver are discussed. Next, the results and statistical analysis are presented and compared to the previous works. We conclude with insight on the suitability of this model for simulating the Martian environment, and how the model may be used to represent other situations. We discuss additional ideas on improving the model in the future.

1.2 Previous Investigations and Statistical Methods

To date, many of the models of Martian methane plumes have concentrated on general circulation models and plumes on planetary scales (see Mischna et al. (2011)). A rover mission to Mars would not be covering the entire planet, but only a small region. The Mars Exploration Rovers were designed for a mission lifetime of 600 meters, although they have well surpassed that distance. Furthermore, models of methane plume distributions estimate that measurements which are not directly in the plume path would need to be made within 100 meters of the plume axis to be discernible from background levels of methane (Olsen and Strong, 2012). This means that a model of local methane plumes are needed to achieve the goal of creating a simulation environment for testing algorithms for a Mars Methane mission. In these local methane plumes, the general planetary circulation which is used as the forcing (advection) function is no longer applicable. Instead, a turbulent environment is more representative of the situation which a robotic rover would find itself in while seeking the methane source.

Many investigations on the structure of turbulent plumes exist. Well known characteristics of odor plumes include the tendency to meander with instances where local concentrations are much higher than the time mean (Murlis et al., 1992). Turbulence can be defined by the nature to create rotational, diffusive and stochastic effects, where a single particle would be observed to wander throughout an area of influence whose

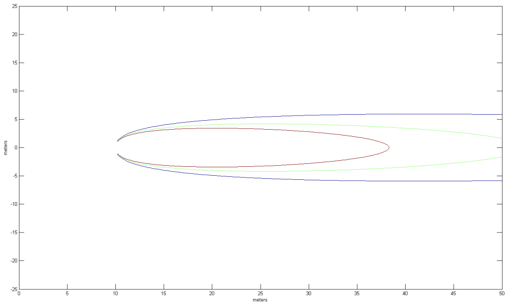

Figure 1.1: **Sutton Contour** A contour map of the Sutton model used for comparison to the model presented.

descriptive length is constantly increasing (Lumley and Panofsky, 1964). This turbulence causes patches of 'clean' air in the plume where concentrations are indistinguishable from background levels. Intermittency is defined as the percentage of time where concentrations are below a defined threshold. Intermittency can be caused by both the meandering and the patchiness of the plume and in tests of several minutes care must be taken to ensure that high values are descriptive of the plume and not the local wind pattern during that time (Murlis et al., 1992).

In order to quantify the characteristics of an odor plume just mentioned, Jones (1983) adapted the statistical methods that Chatwin (1982) used to describe puffs of gas. Jones used these statistics to describe the results of his experiments with turbulent plumes. Farrell et al. (2002) used the same statistical methods to characterize their filament-based model of an odor plume and to compare their model to the experimental results of Jones. We use many of the same statistical methods as these two authors for the ability to compare our model to both past experimental and simulated results.

1.2.1 Long Term Statistics

Time-averaged plumes are generally modeled as a Gaussian plume, of which there are many variations. Of the more popular models is one proposed by Sutton (1953). Since plume dynamics and the movement of a Mars rover are on short time scales, the Gaussian model does not capture enough detail for our uses. However, the realism of our plume can be shown if the long-term average of the model closely replicates the Sutton model. The Sutton model and contour map are shown in Equation 1.1 and Figure 1.1 respectively.

$$C = \frac{Q}{2\pi S_y S_z u} \exp\left(-\left(\frac{y^2}{2S_y^2} + \frac{z^2}{2S_z^2}\right)\right) \tag{1.1}$$

In equation 1.1 Q is the source strength in [kg/s], u is the wind speed in [m/s], S_y and S_z are the dispersion in the y and z direction respectively [m^2/s]. The common expressions for S_y and S_z are shown in Equation 1.2, where C_y and C_z are constants with appropriate units and n is a unitless parameter which governs the shape of the plume. Oftentimes, $n = 1$ is the best match to plumes seen in nature.

$$\begin{aligned} Sy &= 0.5 C_y x^{(2-n)/2} \\ Sz &= 0.5 C_z x^{(2-n)/2} \end{aligned} \tag{1.2}$$

The concentration at a position $\mathbf{p}$ and time t is denoted as $C(\mathbf{p}, t)$. To compare the average concentration of the plume to the Sutton model, the initial period of time where odor is populating the simulation area is ignored. The expression for the mean concentration field is shown below with the time where the odor

Distance Downwind		2m	5m	10m	15m
Jones	$\bar{\Gamma}$ [nC m^{-3}]	4.21	0.525	0.239	0.159
	$\tilde{\Gamma}$ [nC m^{-3}]	28.4	5.33	1.46	0.549
Farrell	$\bar{\Gamma}$ $[\frac{\text{molecules}}{\text{cm}^3}]$	698.01	232.22	69.38	40.48
	$\tilde{\Gamma}$ $[\frac{\text{molecules}}{\text{cm}^3}]$	1494.0	655.4	237.3	136.9

Table 1.1: **General and Conditional Mean Data**: Data collected by Jones during his experiments on an ionized-air plume and from Farrell et al on their filament-based plume model. In both cases the conditional mean is greater than the general mean due to the removal of zero-concentration events from the conditional mean. Also, in all four cases the mean decreases as the sensor's position is further away from the plume.

is well mixed denoted as t_m and the final time of the simulation, t_f. Contour maps of the results will be compared to Figure 1.1.

$$\bar{C}(\mathbf{p}) = \frac{1}{t_f - t_m} \int_{t_m}^{t_f} C(\mathbf{p}, \tau)\delta\tau \tag{1.3}$$

1.2.2 Amplitude Statistics

Jones' experiment consisted of placing four sensors at discrete locations inside the atmospheric plume located in the nominal wind direction; 2, 5, 10 and 15 meters downwind from the source. Data was collected from these four locations throughout the entire experiment. The concentration information used for the statistical analysis are denoted as $\Gamma(\mathbf{p}, t)$. Since there are many stochastic processes represented in the model multiple runs of the simulation are compiled together. Where distinction between multiple experiments is needed, the letter 'r' will represent the experiment as in $\Gamma\ ^r(\mathbf{p}, t)$. The mean concentration recorder by a sensor at a particular location is denoted as $\bar{\Gamma}(\mathbf{p})$.

$$\bar{\Gamma}(\mathbf{p}) = \frac{1}{t_f - t_m} \int_{t_m}^{t_f} \Gamma(\mathbf{p}, \tau)\delta\tau \tag{1.4}$$

Jones noted that the average quantity of the plume matched closely with the statistics when the integral was only calculated during the times when the sensor was in the plume (i.e. the concentration was above a defined threshold, γ). We denote this conditional case as $\tilde{\Gamma}$. Table 1.1 summarized the mean data from both Jones and from Farrell et al. As expected, the conditional means were greater than the general means for each location, which is accounted for by the removal of zero-concentration measurements from the average.

$$\tilde{\Gamma}(\mathbf{p}) = \frac{1}{t_f - t_m} \int_{t_m}^{t_f} \Gamma(\mathbf{p}, \tau)\delta\tau \ \text{ when } \Gamma(\mathbf{p}) > \gamma \tag{1.5}$$

Five additional parameters are used to describe the plume. The n^{th} central moment, denoted as $M_n(\mathbf{p})$ (see Equation 1.6), defines the standard deviation (σ_Γ), skewness (S_Γ), and kurtosis (K_Γ) for n = 2,3,4 respectively, and are normalized so they can be compared across multiple experiments. The peak-to-mean ratio ($\hat{\Gamma}/\tilde{\Gamma}$) is another parameter, where $\hat{\Gamma}(\mathbf{p}) = \max(\Gamma(\mathbf{p}))$. The last metric used is intermittency which is denoted as I, and is the percentage of time where $\Gamma(\mathbf{p}, t) \leq \gamma$, where γ is the same threshold as defined previously.

$$M_n(\mathbf{p}) = \frac{\left(\frac{1}{t_f - t_m} \int_{t_m}^{t_f} \left[\tilde{\Gamma}(\mathbf{p}) - \Gamma(\mathbf{p}, \tau)\right]^n \delta\tau\right)^{1/n}}{\tilde{\Gamma}(\mathbf{p})} \tag{1.6}$$

		σ_Γ	S_Γ	K_Γ	$\hat{\Gamma}/\tilde{\Gamma}$	I(%)
Jones	2m	12.6	4.95	30.2	36.4	85.2
	5m	2.24	7.18	66.6	78.2	90.1
	10m	0.818	8.82	129	112	83.7
	15m	0.346	5.38	42.1	43.5	71
Farrell	2m	2064	4.53	5.81	14.33	53.28
	5m	958	7.75	11.2	43.06	64.57
	10m	339	11.13	18.82	144.14	70.76

Table 1.2: **Amplitude Data**: Unfiltered data collected by Jones during his experiments on an ionized-air plume and from Farrell et al on their filament-based plume model. The five parameters listed here are the standard deviation, the skewness, the kurtosis (the 2nd, 3rd and 4th moments respectively), the peak-to-mean ratio and the intermittency. Notice that the trends for each parameter with distance are similar between the model and the experiment. Farrell did not publish results for the 15m position, probably because in Jone's experiment that sensor did not follow the trend set by the three closer sensors. However, the model of Farrell does not well match the intermittency seen in Jones' experiment. Creating the intermittency from the experiment as shown above (85% throughout) was a challenge faced during the design of the model presented in this paper as well.

Jones' analysis of his experiment consisted of running the data collected from each sensor through a low pass filter with different bandwidths to examine the effects on the five parameters mentioned above. In addition, he computed the results without filtering. Table 1.2 shows the results from Jones for all the positions and Farrell for three positions (Farrell only published results for the three positions shown) for the unfiltered case. The results for the filtered cases are not shown here to due to space constraints but can be found in (Jones, 1983) and (Farrell et al., 2002).

1.2.3 Temporal Statistics

When insects use odor plumes to seek out mates, generally they spend lots of time flying inside the plume, but where there is no detectable amount of odor. Indeed, many plumes are characterized as a group of puffs with much 'clean' air in between. A useful metric for describing this structure is the distribution of the lengths of time where the sensor is measuring above a set threshold, and the distribution of time it takes in between these measurements. Equation 1.7 shows how the experiment can be broken down into discrete quantities of time inside a puff and time inside a gap between puffs. In our model we begin timing only after the first detection event above threshold, hence the approximation in the equation. Jones presents sets of temporal statistics with two thresholds one order of magnitude difference. Although not included within this paper, qualitative comparisons will be made in section 1.4.

$$\sum_{i}^{N_p} t_{p,i} + \sum_{j}^{N_g} t_{g,j} \approx T \tag{1.7}$$

1.3 Model Overview

The concentration at a point in space and time will vary due to reactions which either release or destroy the substance, advection which carries the plume as a whole downwind, and molecular and turbulent diffusion which is responsible for changing the shape of the individual puffs which the plume is made up of. The diffusion-advection-reaction (DAR) equation models these dynamics over time. The two-dimensional diffusion-advection-reaction equation is shown as Equation 1.8, where C is the concentration of methane and is a function of position and time ($C(\mathbf{p}, t)$), D_x and D_y are the molecular diffusion constants in the x and y direction respectively, u_x and u_y are the instantaneous wind speeds in the x and y direction respectively. Q is the rate of methane produced or destroyed at that point in space due to whichever reaction process (environmental or biological) occurs.

$$\frac{\delta C}{\delta t} = D_x \frac{\delta^2 C}{\delta x^2} + D_y \frac{\delta^2 C}{\delta y^2} - u_x \frac{\delta C}{\delta x} - u_y \frac{\delta C}{\delta y} + Q \tag{1.8}$$

The partial differential equation is numerically integrated over time to solve for the concentration at any given location in the simulation area. Boundary conditions on the solver are such that the concentration one-unit distance outside the control boundary is equal to the concentration at the boundary. This allows for the calculations of the necessary gradients. The wind vector $\mathbf{u}$ contains all the wind contributions, and is made up of three components; $\mathbf{u} = \mathbf{a} + \mathbf{v} + \mathbf{t}$. These three components are the advection ($\mathbf{a}$), which is a large scale process which is responsible for moving the entire plume; a medium scale function ($\mathbf{v}$) which is responsible for mixing the individual puffs of methane, and a small scale turbulence ($\mathbf{t}$) which is responsible for the individual motion of the methane puffs.

A number of simplifications have been made to allow for the efficient solving of the DAR equation above.

1. As a Martian rover is a surface mobility platform with no ability to changes its vertical position, the model is in two dimensions only. As of consequence the simulation area is considered flat ground and no perturbations in the wind due to uneven ground or obstacles (including the vehicle) are taken into account.

2. As discussed earlier, one of the anomalies in the methane measurements on Mars is the quick time scale with which methane is destroyed. Although there are many proposals for processes which could explain methane destruction on quicker time scales, the true nature of the destruction remains a mystery. In addition, the time scales of the simulation will be much smaller than even these relatively 'quick' methane lifetimes. Therefore, no destruction process is modeled. Instead, methane is carried out of the simulation environment due to the wind, but no methane is brought into the simulation area due to potential upwind sources. This imbalance acts as our sink and stabilizes the solver.

3. Although multiple methane sources can easily be added to the simulation, a single source is used for validation in this paper.

4. The wind model to be presented does not necessarily follow conservation laws. It is not meant to be a replicate for real wind patterns on Mars, however it is meant to produce methane distributions whose statistics match those which we would expect for those situations.

1.3.1 Model Functions

The methane source location and radius are defined in the simulation parameters. Three options for releasing methane at the source were discovered and analyzed. The first method was a continuous source which changed levels based on a variable's random walk processed through an absolute sine function for bounding. The second method was a discrete release which would turn on or off depending on two random input signals and a clock, and would act like a J-K flip flop. At a certain frequency the signs of the two signals would determine whether the state of the source would turn on, turn off, stay the same, or 'toggle' states. The third option was a discrete puff where instantaneous release of methane would occur at a given frequency. The continuous source produced a snake-like pattern, but did not produce the patchy plume sought from the model. The J-K flip-flop mode created the patchy nature we were looking for, but the statistics did not match those of Jones. The discrete puffs of methane did create the distribution desired and the frequency of 3Hz was used for all the statistics shown.

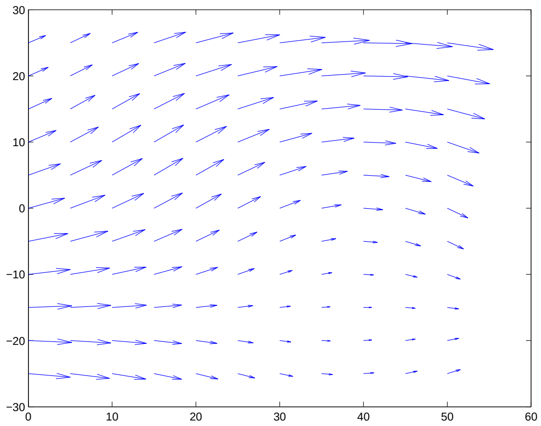

Figure 1.2: **Advection Profile** The results of the nominal advection in combination with the perturbations from the Fourier surface. The nominal wind is in the positive x-direction.

As discussed previously, the wind model is made up of three parts: advection, vortex, and turbulence. Each of these represents a transportation scale; advection affects the plume as a whole, vortex effects the puffs as individuals, and turbulence effects the particles of methane. The advection force varies its magnitude and direction both in time and position which causes the plume to form a sinuous shape. Vortex are local, circular wind patterns which change the shape of the puffs and move them cross-wind simultaneously. Turbulence is discrete, stochastic noise added to the system.

The advection function consist of a nominal direction and speed which is varied with position and time. The nominal direction is allowed the vary with time from $\pm 30^o$ with the mean direction corresponding to the nominal downwind direction. The wind varies with position by superimposing effects from a random function which varies continuously with time. This function is formed by creating a three-dimensional surface. Wind direction follow lines of constant altitude on the surface and the strength corresponds to the gradient. Equation 1.9 shows how the two components of the advection vector are determined.

$$a_x(x,y) = \frac{-\delta Z(x,y)}{\delta y} \qquad\qquad a_y(x,y) = \frac{\delta Z(x,y)}{\delta x} \tag{1.9}$$

This surface is formed from using the Fourier series seen in Equation 1.10. The parameters of the function are varied by filtering white Gaussian noise through the filter $H(s) = \frac{G}{s^2+as+b}$. The effects of advection can be seen in Figure 1.2.

$$\begin{aligned} Z_f(x,y) = &\sum_{n=1}^{N} A_n \sin\frac{n\pi x}{L_x} + B_n \cos\frac{n\pi x}{L_x} \\ &+ C_n \sin\frac{n\pi y}{L_y} + D_n \cos\frac{n\pi y}{L_y} \end{aligned} \tag{1.10}$$

Medium scale mixing of methane puffs is modeled by adding 'vortices' to the model. The effects of the vortex are described by a Gaussian pulse surface being formed and using the same method to extract the wind directions and magnitudes. The amplitude and diameter of this surface can be specified but are kept constant throughout the simulation. The vortex position travels along the simulation area according to the advection, that is $\dot{\mathbf{p}}_v = \mathbf{a}$.

Turbulence is added to the base wind in the form of a stochastic change in magnitude of the x and y wind directions. In order to prevent the model from diverging, feedback is used to drive the total wind model with turbulence towards the base wind. It is seen below that the second derivative of the turbulence is calculated by multiplying a gain by a matrix of random numbers on a normal distribution (R), and then is corrected by the feedback of the previous full wind model and the current base wind model. The gains for the feedback are experimentally tuned to ensure the model does not diverge.

$$\ddot{U}^{k+1}_{x,turb} = K_1 R^{k+1}_x + K_2(U^k_x - U^{k+1}_{x,base})$$
$$\ddot{U}^{k+1}_{y,turb} = K_1 R^{k+1}_y + K_2(U^k_y - U^{k+1}_{y,base})$$

1.3.2 Model Solver Limitations

In the explicit form, the difference equation has a stability issue when the time step used is beyond a threshold. This threshold is a function of the coefficients of the equation. This section details the analysis of the stability of the difference equation and the determination of a time step that both satisfies stability while also minimizing computation during simulation runs. Stability of difference equation theorem relies on the coefficients of each C^k_m term in the difference equation being non-negative.The value of the time step is determined by the $C^k_{i,j}$ term. We set the Δx and Δy values to be the same (Δ) since this will make processing the simulation results easier. In addition, the physical diffusion constants will be omni-directional in the 2D space so $D_y, D_x \to D$. If we replace u_x and u_y with the total wind vector, we will compensate for any reference frame coordinates of the vector, plus it helps to compensate for any turbulence or vortex contributions. We set the coefficient of $C^k_{i,j}$ to ≥ 0.

$$\Delta t \leq \left[\frac{\Delta^4}{4\Delta^2 D + 2\Delta^3 u_{max}}\right] \tag{1.11}$$

We therefore choose our time step to be small enough as to satisfy Equation 1.11 above. In order to capture the small scale puffs and gaps in the plume, the resolution of the simulated area must be sufficient. This high resolution in addition to a small time steps can cause computational problems, where creating numerous simulations can take long periods of time. Farrell et al. (2002) strove to create a simulation which could create 100 ten-minute simulations in 24 hours; our model certainly takes longer to run than that.

1.3.3 Sensor Model

The equations used to model the sensor and low-pass filter are given as Equation 1.12. Here, the internal state of the filter is f and y is the output of the sensor. The bandwidth of the filter is α and the threshold γ is the same as defined previously.

$$\begin{aligned} \dot{f}(t) &= -\alpha f(t) + \alpha\Gamma(t) \\ y(t) &= \begin{cases} f(t) & \text{if f(t) } \geq \gamma \\ 0 & \text{otherwise} \end{cases} \end{aligned} \tag{1.12}$$

1.4 Model Analysis

Multiple simulations have been reviewed to ensure that the simulation performs similarly in different initial conditions and with different random number seeds. Here we will discuss the results of one of these experiments which is representative of the entire group. At each instant during the simulation the plume is characterized as sinuous and patchy. The general mean concentration map of the entire simulation however, closely resembles a Gaussian plume model. Figures 1.3a and 1.3b compares the concentration maps between the instantaneous and the time-averaged cases. Figure 1.3a shows isopleth from the time averaged map and a Gaussian plume. The Sutton plume as defined in section 1.2 is used as the Gaussian plume for comparison. Values of 100, 1, and 0.2 are used for Q, K_x and K_y respectively. It is seen that the Sutton model well-approximates the time average plume in the simulation.

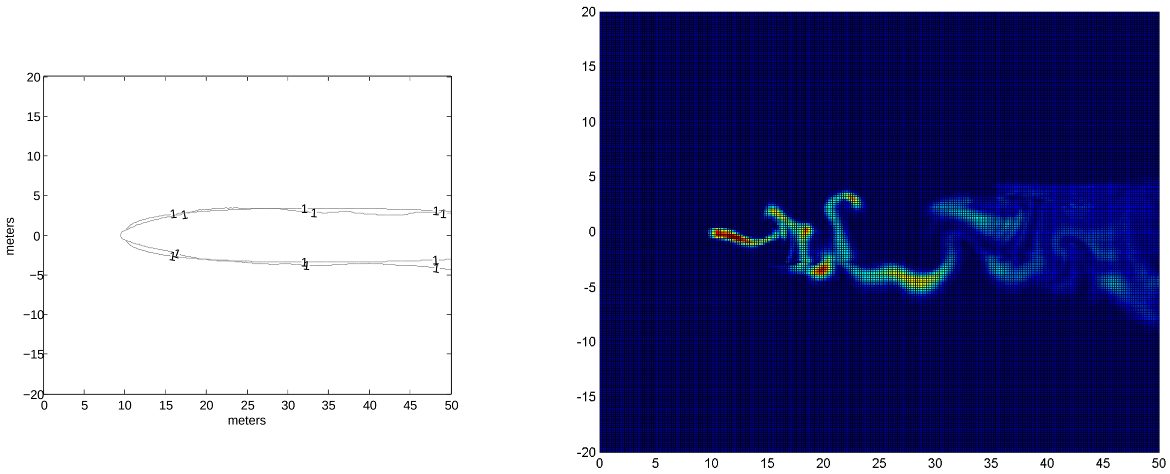

(a) Sutton vs. Presented Model

(b) Snapshot of Present Model

Figure 1.3: **Long Term Average Comparison**: Results from the simulation with the plume source at (10,0). The results presented in (1.3a) are the mean over a ten minute period compared to Sutton's Gaussian model. In (1.3b) a snapshot of the instantaneous plume is shown.

Position	2m	5m	10m	15m
$\bar{\Gamma}$ [kg/m^3]	5.776	2.729	1.801	1.487
$\tilde{\Gamma}$ [kg/m^3]	6.438	4.582	3.121	2.407

Table 1.3: **General and Conditional Mean Data**: Presented is the (general) mean of the simulated measurements of the model at four positions and the conditional 'in the plume' mean.

Table 1.3 presents the general and conditional means which are comparable to the same data given by Jones and Farrell and summarized in Table 1.1. As would be expected, the conditional means are greater then the general mean at each location. The means from the two previous results and the current model are also plotted in Figures 1.4a and 1.4b. The data is normalized to compare between the two models and the experiment based on the results at the 2m position. It is seen that the current model follows the downward trend of the other two plots, but does not match the experimental data as well as Farrell et al's model. This is especially true for the conditional mean. This is a result of the fact that in both Jones' experiment and Farrell's model the intermittency for all positions were fairly similar, whereas in the current model the intermittency at 2m is significantly lower than the other positions. Since this trend greatly affects both means, it is the likely source of the discrepancy.

The amplitude statistics are presented in Table 1.4 for comparison to the unfiltered values summarized in Table 1.2 in addition to the filtered values published in (Jones, 1983) and (Farrell et al., 2002). In consistency with the publications of Jones and Farrel et al, the results are presented for the four positions and six filtering conditions. Trends for many of the parameters fit the trends of Jones' experiment. These trends include a decrease of all parameters as the filter bandwidth decreases and increase of the skewness, kurtosis, and peak-to-mean ratio as the distance from the source increases.

The most obvious trend which the model did not replicate is the consistent levels of intermittency throughout the experiment. The two-meter downwind location had a much lower percentage of intermittency than the other three positions. In Jones' experiment, levels of intermittency did not follow an exact trend and were fairly consistent. Intermittency increased 20% for the three data points given by Farrell et al which

				With low-pass filtering				
	Paramter	Symbol	Unfiltered	30Hz	10Hz	3Hz	1Hz	0.3Hz
2m Downwind	Standard Deviation	σ_Γ	0.551	0.551	0.549	0.544	0.496	0.326
	Skewness	S_Γ	0.195	0.195	0.194	0.182	0.154	0.106
	Kurtosis	K_Γ	0.708	0.708	0.706	0.691	0.617	0.407
	Peak-To-Mean Ratio	$\hat{\Gamma}/\tilde{\Gamma}$	3.10	3.10	3.07	2.97	2.70	2.06
	Intermittency	I(%)	10.5	10.5	10.2	7.5	1.2	0.3
5m Downwind	Standard Deviation	σ_Γ	0.655	0.655	0.655	0.676	0.685	0.514
	Skewness	S_Γ	0.269	0.269	0.268	0.284	0.316	0.239
	Kurtosis	K_Γ	0.823	0.823	0.822	0.847	0.883	0.687
	Peak-To-Mean Ratio	$\hat{\Gamma}/\tilde{\Gamma}$	3.11	3.11	3.09	2.99	3.13	2.67
	Intermittency	I(%)	41.2	41.2	40.7	35.2	19.1	3.1
10m Downwind	Standard Deviation	σ_Γ	0.683	0.683	0.682	0.685	0.664	0.543
	Skewness	S_Γ	0.323	0.323	0.323	0.327	0.331	0.279
	Kurtosis	K_Γ	0.901	0.901	0.899	0.902	0.899	0.798
	Peak-To-Mean Ratio	$\hat{\Gamma}/\tilde{\Gamma}$	3.75	3.75	3.73	3.64	3.46	3.49
	Intermittency	I(%)	43.7	43.7	43.4	39.7	28.8	12.2
15m Downwind	Standard Deviation	σ_Γ	0.688	0.687	0.687	0.684	0.642	0.514
	Skewness	S_Γ	0.361	0.361	0.361	0.361	0.344	0.257
	Kurtosis	K_Γ	0.979	0.978	0.977	0.970	0.921	0.721
	Peak-To-Mean Ratio	$\hat{\Gamma}/\tilde{\Gamma}$	4.29	4.28	4.23	4.04	3.71	3.02
	Intermittency	I(%)	40.7	40.7	40.3	36.9	27.4	11.3

Table 1.4: **Statistical Data for Modeled Plume**: The five statistical parameters; standard deviation, skewness, kurtosis, peak-to-mean ratio, and intermittency, are given for four sets of data describing four locations along the nominal wind position for a ten minute long simulation. The first three parameters are normalized with the conditional mean at that location, with thresholds 5% of the max levels seen at the 2m position.

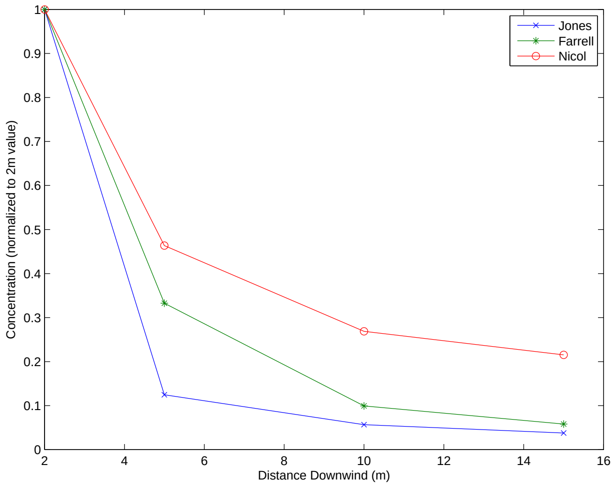

(a) General Mean Comparison

(b) Conditional Mean Comparison

Figure 1.4: **Comparison of Means**: The figures above show the mean concentration over four positions for Jones' experiment, Farrell et al's simulation and the model presented in this paper. All data sets are normalized by that set's concentration at 2m.

was more than double the range of Jones' data for the same distance covered. Once the plume reactes the five meter position, it is well mixed and the intermittency stays very consistent (a range of 3% over 10 meters). Even so, the intermittency was still much lower than that of both the experimental data and Farrell et al's model. The next deviation from the experimental data is the tendency for the standard deviation to increase as distance from the source increases, which is the opposite trend seen in the experiment.

The final difference in results is the lack of deviation from trends at the 15-meter downwind position. In Jones' experiment, the skewness, kurtosis, and peak-to-mean ratio all tend to increase with distance downwind except for the final position (15-meters) in which it decreases. The standard deviation is the only parameter which doesn't exhibit this reversal. Farrell et al do not acknowledge this strange behavior in their analysis of their model, and instead do not publish their results or make comparison at the 15 meter downwind position; their results match the trends up to that point. The results of the current model show that they do not reverse trends at the 15m point for any of the parameters. We can only assume that this is the same results as Farrell et al's model, and although not preferable based on the experimental data, acceptable for validation.

The short-scale analysis is summarized in the histograms of Figures 1.5a through 1.5d for two positions and two threshold levels. Jones published histograms for the 2-meter and 15-meter downwind positions; due to the low intermittency of the 2-meter position, we have shown the results for the 5-meter position instead. In keeping consistent with Jones, the higher threshold is one order of magnitude higher than the lower threshold. In all cases, the puff lengths were generally much smaller than the lengths of time between puffs. This is the main characteristic of the results shown by Jones. In addition, the puff lengths at the higher threshold are much shorter than for the lower threshold, and the gap lengths exhibit the reverse trend. The puff return statistics for the five-meter position do not exhibit the same separation between the two thresholds that the 15-meter position and the results of Jones have. However, the lengths at the high threshold extend into the higher range of time-lengths which would be expected.

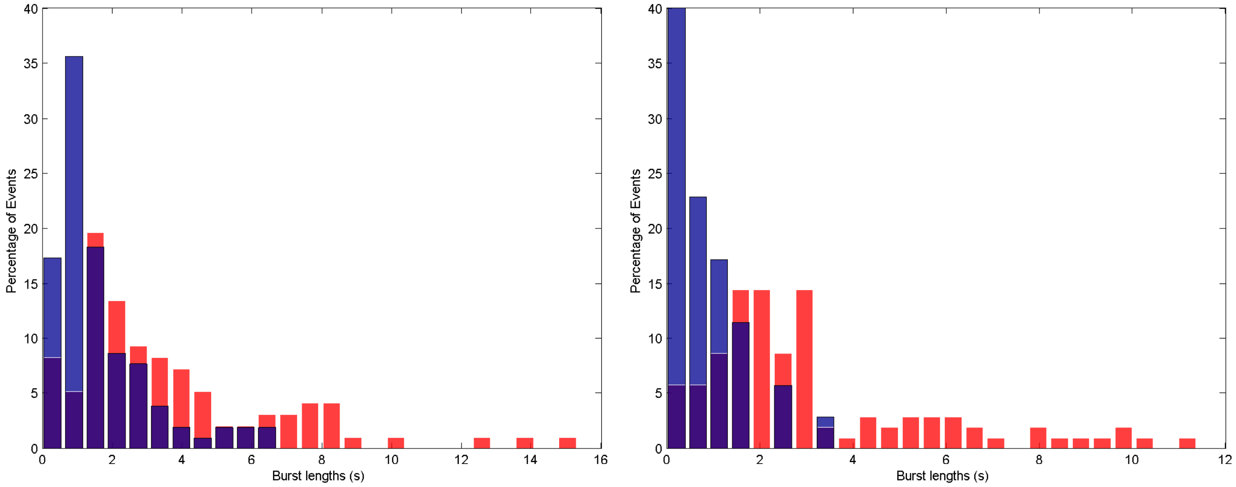

(a) Puff length statistics at 5m downwind

(b) Puff length statistics at 15m downwind

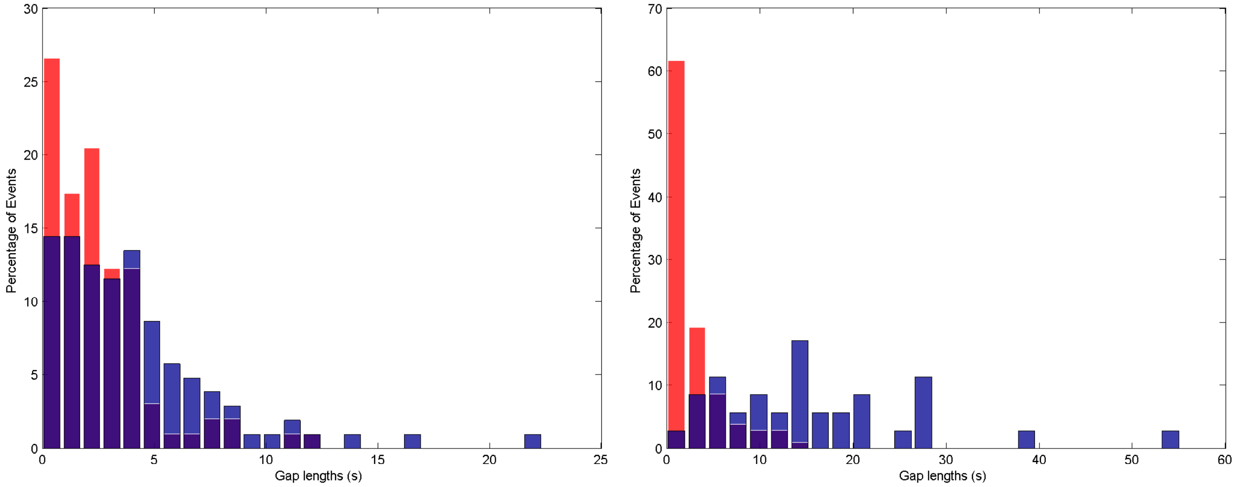

(c) Puff return time statistics at 5m downwind

(d) Puff return time statistics at 15m downwind

Figure 1.5: **Temporal Statistics**; The charts above give the distribution of times for the length of puffs (continuous concentrations above threshold) and the time for a puff to return (continuous time below threshold) at 5m and 15 m downwind.

1.5 Conclusion

Presented is a model for simulating methane plumes on Mars. This model can be used to create scenarios for testing robotic algorithm‘s effectiveness and efficiency at finding the source of the plume. Although the analysis presented here was done for a single source, multiple sources can be incorporated into the simulation with ease. Analysis of our model shows that it is suitable for simulating Martian methane plumes. Although there are some discrepancies between the amplitude statistics for the current model and experimental data, the short-scale data shows that the plume exhibits the characteristics which make plume-tracing difficult, short time spent sensing concentration with large gap times. Furthermore, since the nature of the fine scale Martian methane plumes is currently unknown (and will be until a mission concept like the one presented earlier is deployed), this scheme represents the best environment for algorithm development.

Chapter 2

Enceladus

2.1 Introduction

Interest in the Saturian moon Enceladus was first attributed to its orbital position in the densest part of Saturn's E-ring. Due to the instabilities of the models of the E-ring, Enceladus was thought to act as the source of the material (Jurac, 2001). The Voyager mission included a flyby of the moon's northern hemisphere and viewed a diverse geography with large number of creators in the north with less creators in the south and on plains. This diversity in crater density suggested some form of geological activity inside the body (Porco et al., 2006), furthering interest in its study. The Cassini spacecraft, which was launched in 1997 and arrived at Saturn in 2004, was able to prove once and for all that Enceladus is the source of the E-ring by observing eruptions of water gas and dust particles out of the south polar region of the moon.

Since its first insertion into orbit about Saturn, the Cassini spacecraft has made numerous flybys of Enceladus. Many of these were scheduled as part of Cassini's first and second extension missions. Cassini has multiple instruments on board which are able to take in situ measurements of Enceladus' interior through sampling the plume during flybys. These instruments include the Imagining Science Subsystem (ISS), the Visual and Infrared Mapping Spectrometer (VIMS), the Composite Infrared Spectrometer (CIRS), the Cosmic Dust Analyzer (CDA), the Ion and Neutral Mass Spectrometer (INMS), and the Ultraviolet Imaging Spectrograph. Cassini also employs its magnetometer to measure the distortion in Saturn's gravitational field.

The south polar terrain, as seen in Figure 2.1, consists of a fractured province. Long, distinct fissures running 130 km in length through the south polar region named 'tiger stripes' are four distinct fissures running 130km long, 2km wide, with ridges 100m high on each side (Porco et al., 2006). These tiger stripes are the most prominent fractures in the south polar region, and are individually named Damascus, Baghdad, Cairo, and Alexandria. Spitale and Porco (2007) used images from the ISS to triangulate the position of the most prominent jets which were able to be identified in the images (see Figure 2.2) and these locations corresponded to locations on the tiger stripes. These locations are denoted in Figure 2.1 as the white circles with the individual sightings marked as diamonds in different colors.

Cassini measurements with the Ion and Neutral Mass Spectrometer (INMS) indicate a plume whose composition is mostly water (91 ± 3%) with carbon dioxide (3.2 ± 0.6%), nitrogen or carbon monoxide (4 ± 1%) and methane (1.6 ± 0.4%) (Waite et al., 2006). Quantities less than 0.5% of ammonia were measured. The measurements were unable to determine which compound, nitrogen or carbon monoxide, was measured at the 28 dalton point. Waite et al. (2006) estimated the mass loading of the plume to be 90 kg/s based on INMS reading. Measurement of the plume during a stellar occultation with the Ultraviolet Imaging Spectrograph (UVIS) lead Hansen et al. (2006) to estimate the mass loading at a lower limit of 150 kg/s, which was confirmed through modeling by Tian et al. (2007). Current estimates of the ejection rate of the plume is between 500 and 750 kg/s, varying with the position in Enceladus' orbit.

Spencer et al. (2006) first reported a thermal anomaly of Enceladus' tiger stripes, measured with the

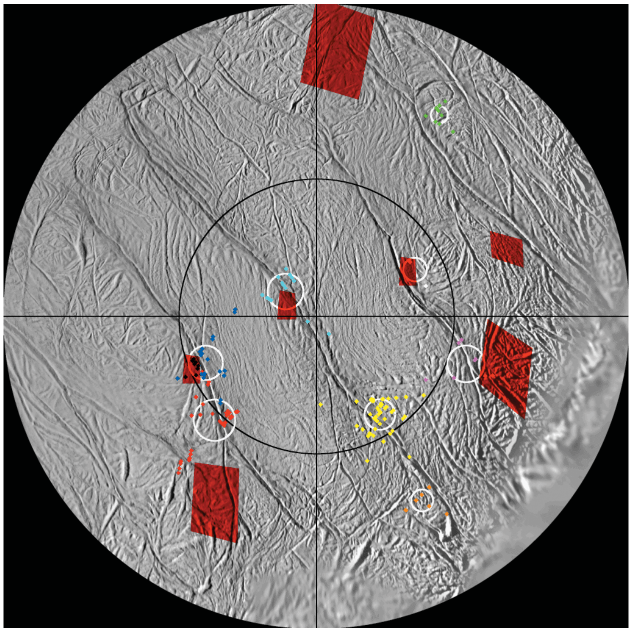

Figure 2.1: **South Polar Terrain Showing Tiger Stripes**: The south polar terrain is shown with the tiger stripes and hot spots identified by Spencer et al. (2006) as the red squares and the eight main source locations identified by Spitale and Porco (2007) as the white circles. Courtesy Spitale and Porco (2007)

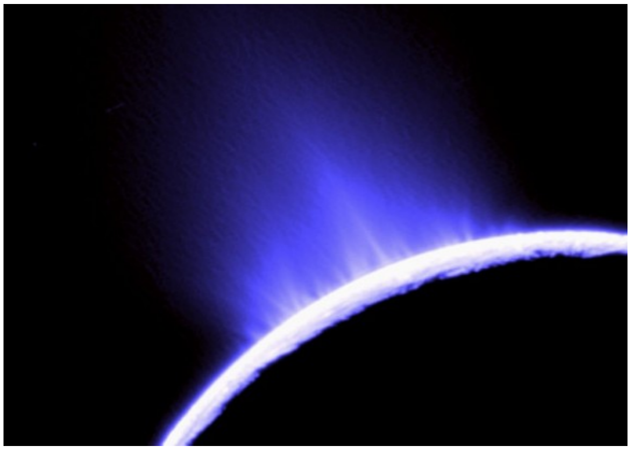

Figure 2.2: **Enceladus Jets Forming Plume**: Cassini image of Enceladus showing the many individual jets of fine icy particles erupting from the south polar region and forming the plume. Courtesy NASA/JPL

Cassini Infrared Spectrometer (CIRS). Temperatures measured much higher than expected, as well as from the rest of the moon. Seven hot spots were recorded with the maximum temperature at 157 ± 24 K. The estimated total heat radiated from the south polar terrain was 5.8 ± 1.9 GW. Spencer et al. (2006) estimated that the minimum distance from the surface to a liquid reservoir would be 40 meters based on conduction heat transfer. However, it is more likely that heat is transferred through convection from the jets, increasing the potential depth of the liquid reservoir. Of the eight sources located by Spitale and Porco (2007), four match identically to a thermal hot spot, with two other sources being in the near vicinity of other hot spots.

Postberg et al. (2009) have stated that the particles sampled from the E-ring and plume, imply that there is a subsurface ocean on Enceladus which is in contact with its rock core. Nimmo et al. (2007) proposed that shear stresses could cause local pockets of liquid water near the surface, but there would also need to be a large subsurface ocean. Tobie et al. (2008) did one of the most extensive studies of the effect of tidal heating on Enceladus. They concluded that there needed to be a decoupling layer between the south polar terrain ice and the core of the moon for the dissipation of the tidal heat to occur as observed. A global subsurface ocean is not required, however, as long as the ocean covers the majority of the south polar region province. This liquid layer could be one of the most accessible locations in the solar system where life could possible exist.

The majority of habitability studies conducted to date focus on Europa as the most likely location for finding extraterrestrial life in the solar system (Reynolds et al., 1983; Greenberg et al., 2000; Chyba and Phillips, 2001). Like Enceladus, Europa is thought to experience tidal heating which forms a large subsurface ocean between its ice crust and rock core (Hoppa et al., 1999). The disadvantage to studies of Europa is the large ice crust which is thought to be hundreds of kilometers thick which separates the possible habitat from study. Even if signs of life were to permeate through the ice to the surface, Europa is blasted with radiation from the Sun contaminating the top meters of ice. Therefore the minimum effort to detect life would consist of drilling meters into the ice (Parkinson et al., 2008). In contrast the geysers on Enceladus' southern polar region allow for an in situ measurement of the interior composition. Indeed, many models of Enceladus' interior have already been derived from the composition of the plume as measured by Cassini. In addition, there is evidence to support that the material that falls to the moon's surface as it travels through the E-ring makes its way into the interior of the body. Thus it is proposed that water particles erupted from the jets make their way into the E-ring of Saturn. There, they act with radiation and some particles turn to hydrogen-peroxide (H_2O_2). As Enceladus travels through the E-ring, it collects E-ring particles on its surface including those which may have formed in the E-ring; these particles permeate through the ice crust into the interior. Having a geochemical cycle as would greatly increase the likelihood of life developing (Parkinson et al., 2008).

Although much knowledge has been gathered through the in situ measurements of Enceladus' plume, key questions about the habitability of its subsurface oceans and the possible presence of life can only be answered with probes into the subsurface. Planetary penetrators are a potential vehicle for such a probe. Planetary penetrators are a self-contained spacecraft vehicles which act as high-speed landers with the goal of traversing a distance through the solid material which they impact. This type of spacecraft is typically characterized as low-mass (3-10kg), high impact velocities (300m/s), and a long cylindrical shape with a nose cone. One operation method for a penetrator mission is to release the penetrator from a main spacecraft during a flyby of a science target and, using a propulsion system, decrease velocity to allow the gravity of the target body to deorbit the spacecraft. This could be done with a single deorbit thruster which is pointed in the direction needed to continue to negate the forward velocity. Three-axis attitude control would be necessary to have a full range of controllable thrust directions.

The first proposal for a planetary penetrator was in 1974 by the Sandia Labs in New Mexico at the same time that Young developed his first set of empirical penetration equations. To date, there has not been any successful penetrator missions, although many have gone through detailed design and few launch attempts were made. The Mars-96 mission contained two penetrators on board. However, the mission was lost when the launch vehicle failed trying to leave Earth's atmosphere, causing the entire spacecraft to crash back into Earth. The Japanese Lunar-A mission was a lunar penetrator and began in the mid-90's, however was never launched and was formally canceled in 2007. The Deep-Space 2 micro-probes were on board the Mars Polar

Lander but both the lander and the probes were lost during entry into the Martian atmosphere.

As was discussed previously, the targeting requirements for this proposed mission are much tighter than for other lander missions. In addition, the actual target location is unknown and must be estimated in real-time throughout the descent. In a traditional penetrator system, the penetrator is deorbited through the use of reverse thrusters and is then released to free-fall to the surface. We propose an additional control mode where the penetrator is free-falling, however lateral motion is actuated to fine-tune the positioning of the spacecraft. This ability to vector in forward flight (VIFF) allows the fine control of the spacecraft, increasing the likelihood of hitting its target. However, it means that an additional control law be put in place for the lateral motion.

The eight main locations where jets of material were observed throughout the close-range flybys of *Cassini* provide an initial target for a penetrator mission whose purpose is to penetrate into the subsurface ocean. High resolution photos of these areas during subsequent flybys revealed that these plume sources are actual characterized by numerous jets on the order of tens of meters in diameter spread over square kilometers. The diameter of the geyser defines the targeting accuracy of the mission. In order to get the penetrator to have a targeting ability on the order of meters, the first assumption that needs to be made is that the target location is known. Constantly updating the estimate of the target location is necessary for the success of the mission. We propose a system based on the recurrent neural network which actively fuses the localization and control of the spacecraft into one system. The input to this system will be a measurement of the water density and the average particle size. Although the jets will diffuse into the overall plume, we will attempt to extract information about the jets from the sequence of measurements taken.

In order for the plume to be valuable for our purposes we do not concentrate on developing a model which will gave the same measurements of phenomenon as Cassini. Instead, we focus on the following characteristic:

- Representative of the plume structure on the large scale as well as the small scale where the jets are most distinguishable. Where most models only concern themselves with representing the plume on the large scale (far away from the moon where the jets have diffused into a single plume) we are concerned with penetrating into the individual jets which requires a small scale model. Therefore the model must consist of the multiple jets instead of single sources or only the eight sources noted by Spitale and Porco (2007). Despite the concentration on the small scale plume, the large scale plume must develop consistent with the Cassini measurements.
- There are numerous proposed jets throughout the tiger stripes, although theories are that the jets are more numerous and cluster in the eight regions seen by Spitale and Porco (2007). Because the exact structure of the plume is still unknown, a stochastic component of the model is included to provide for numerous scenarios. This means that multiple scenarios can be crated with jets with different combinations of location and strengths. Each scenario should result in the same trends as seen in the Cassini data, but do no need to match exactly.
- The plumes have been observed to deviate over time, and some correlation with the tidal stresses have been observed. Insignificant numbers of measurements at the same true anomaly has limited the ability to confirm correlation. The distribution of jets over the tiger stripes and their relative strengths must be impacted by the desired true anomaly of the moon during the mission.
- Although we have just stated that the plume deviates over time, the proposed penetrator mission has a time scale which is much shorter than the cycle length of the deviations of jet activity. A dynamic plume model would change insignificantly over the time frame of the mission. Therefore, we develop a static plume model for our simulations.

This article will detail the current model used for testing navigation algorithms. The next section will detail the models of previous authors and the validation each author used. We then describe our model; the model for the jets and the function used to randomly determine their position and the source strengths. We then use the previous models and Cassini data to validate the large scale plume created by our model.

2.2 Model Description

The plume of Enceladus is formed by the diffusion of multiple geyser jets erupting on the tiger stripes in the South Polar Terrain (SPT) of the moon. Eight sources of high ejection rates were located by Spitale and Porco (2007). With closer flybys provided better resolution of the SPT it was seen that many more jets existed along all four tiger stripes. Many of the models in the literature disregard these minor sources and only use the eight well-viewed sources. These models have proved to be representative of the overall plume at altitudes where Cassini is conducting its flybys. However, for a descent mission which relies heavily on the fine structure of the plume, we model multiple jets. The plume concentration is the sum of the effects of all jets.

For each flyby of Cassini, the plume has been observed to be in a different form. Attempting to create models which replicate the measurements of Cassini result in different emission rates for the sources for each pass, and imagery has failed to show consist eruptions for each jet during every flyby. The activations of particular jets were shown to correlate with the expected tidal stresses of the region were the source is located. When the source is in tension the jets seem to be activated, but when the sources are in compression they tend to be stagnate.

As one of the goals of the model is to be able to produce high number of different scenarios, we randomly distribute the jets along the tiger stripes defined by a probability distribution function (PDF). The PDF is created by defining the percentage of jets which are to be located at the eight well-observed sources; the remaining which are normally distributed about the tiger stripes. Each jet is given the same strength potential (the maximum ejection rate) and therefore the percentage of jets at the well-observed source locations is proportional to the percentage of ejection material coming from these same sources. Further variability is added by alternating the strengths of the jets as a function of the normal stresses acting on the tiger stripe at the position of the jet. Although the relationship between ejection rate and stresses is not solved, two relationships have been proposed by Hurford et al. (2009): the first relation has the ejection rate proportional to the normal stress when positive (with ejection rate equaling the potential at the maximum stress), the second relation has the maximum ejection rate at the instant the jet switches from compression to tension and dying off. In both cases, a compression strength results in zero ejection from the jet.

The tidal stress model used to describe the stresses acting on an orbiting body due to the non-circular orbit of Enceladus is adopted from Nimmo et al (see supplementary material). This is a simplified model but matches well with the more developed SatStress created by Wahr et al. (2009). These tidal stresses as defined by Equations 2.1 - 2.3 are a function of the position and orbital position, represented by the colatitude (θ), the longitude (ϕ) and the mean anomaly (m). The colatitude is positive in the south direction (0 - π) and the longitude is positive in the west direction (0 - 2π). A list of the other parameters and the values used can be seen in Table 2.1.

$$\begin{aligned}\sigma_{\theta\theta} =& c_1 e(-\cos m[3l_2 \sin^2\theta + c_2\Delta(3\cos^2\theta - 1)] \\ &+ .5[l_2(1+\cos^2\theta) + c_2\Delta\sin^2\theta][-\cos(2\phi+m) + 7\cos(2\phi-m)]) \quad (2.1)\\ \sigma_{\phi\phi} =& c_1 e(-\cos m[-3l_2 \sin^2\theta + c_2\Delta(3\cos^2\theta - 1)] \\ &+ .5[-l_2(1+\cos^2\theta) + c_2\Delta\sin^2\theta][-\cos(2\phi+m) + 7\cos(2\phi-m)]) \quad (2.2)\\ \sigma_{\theta\phi} =& c_1 e l_2 \cos\theta[\sin(2\phi+m) - 7\sin(2\phi-m)] \quad (2.3)\end{aligned}$$

To determine whether the tiger stripes are in a state where eruptions may occur, the normal and shear stresses are resolved from the primary stresses above. The shear (τ) and normal (σ) stresses are a function of the orientation of the fault line at the location in question (Equations 2.4 and 2.5 respectively). The angle between the fault and constant line of longitude is defined as β, and $\beta' = \beta - \pi/2$.

$$\tau = .5(\sigma_{\phi\phi} - \sigma_{\theta\theta})\sin 2\beta' + \sigma_{\theta\phi}\cos 2\beta' \quad (2.4)$$

$$\sigma = \sigma_{\theta\theta}\cos^2\beta' + \sigma_{\phi\phi}\sin^2\beta' + \sigma_{\theta\phi}\sin 2\beta' \quad (2.5)$$

Parameter	Symbol	Value
Primary Mass	M	5.7 $\times 10^{26}$ kg
Gravitational Constant	G	6.67×10^{-11} m^3/kg s^{-2}
Moon Surface Gravity	g	0.11 m/s^2
Moon Radius	R	252.1 km
Moon Semi-Major Axis	a	238000 km
Eccentricity	e	0.0047
Love Number	h_2	0.2
Love Number	l_2	0.04
Lame Parameter	λ	6.8 MPa
Lame Parameter	μ	3.5 MPa
Parameter	z	$\frac{3GMR^2}{2a^3}$
Parameter	c_1	$\frac{z\mu}{gR}$
Parameter	c_2	$h_2 - 3l_2$
Parameter	Δ	$\frac{3\lambda+2\mu}{\lambda+2\mu}$

Table 2.1: Parameters in Stress Model

Jets are placed so that M percentage of the total jets (N) are placed in proximity to the location of the eight source locations, with the remaining jets being uniformly distributed throughout the tiger stripes. Figure 2.3 shows the model of the tiger stripes with the eight plume sources marked. The source strength of the jets are given as a function of the normal stresses on the tiger stripe at the location where the jet is. The strength of each jet is than normalized such that the total mass discharge between 500 and 750 kg/s. The exact value for the total discharge is a function of how many of the jets are in compression.

Jet Models that have been developed to replicate in situ plume measurements by Cassini fall into two main camps. Saur et al. (2008) develops a Gaussian model of the plume, and analyzes its ability to replicate the magnetic field observations by Cassini's magnetometer during the E0, E1 and E2 flybys. He uses his model as both a single source model with the source location being the south pole, and a multi-source model using the eight sources located by Spitale and Porco (2007). Jia et al. (2010) use a similar but different form of a Gaussian plume while also studying the magnetosphere. The Saur et al. (2008) model is used again by Fleshman et al. (2010) and Kriegel et al. (2009) in studying the plasma interaction of Enceladus with magnetometer data. The model suggested by Saur et al. (2008) is shown in Equation 2.6. The other common form of the plume model is derived from Maxwellian velocity distribution at the source(s) (Tenishev et al., 2010; Dong et al., 2011).

$$n(r,\theta) = n_0 \left(\frac{R_E}{r}\right)^2 \exp\left[-\left(\frac{\theta}{H_\theta}\right)^2\right] \exp\left[-\frac{r-R_E}{H_d}\right] \tag{2.6}$$

A Gaussian jet model is employed for our purposes, albeit in different form than Equation 2.6. Equation 2.7 shows the model for a single jet where Q is the jet emission rate, u_c is the characteristic velocity, k_c is the diffusion constant, and Ψ_0 is the size of the jet. The concentration is a function of position, which is described by the altitude (h) and the radius (R) from the vector normal to the surface at the jet location. This model is derived from plume models which propagate downwind. One of the main assumptions is that the majority of the particles in the plume eventually escape Enceladus' sphere of influence and enter to the

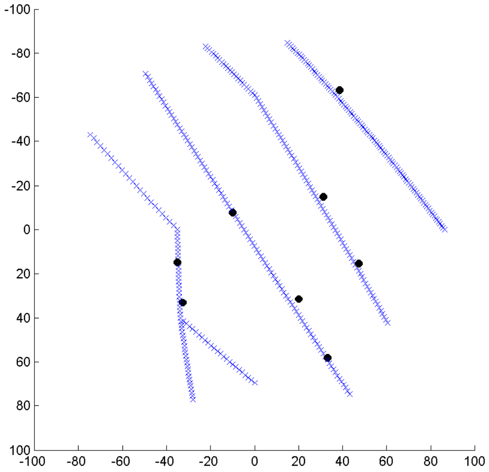

Figure 2.3: **Model of Tiger Stripes**: The blue crosses represent the modeled boundary of the tiger stripes for comparison to Figure 2.1. The black dots indicate the center of Spitale and Porco's eight identified main sources.

E-ring, only to be replaced by new particles.

$$C = \frac{Q}{2\pi u_c \Psi_r} \exp\left(-\frac{R^2}{\Psi_r}\right) \tag{2.7}$$

$$\Psi_r = \Psi_0 + \frac{k_c h}{u_c} \tag{2.8}$$

Figure 2.4 shows an example of the random distribution of jet locations with N = 100 and M = 0.5. The results match well to the sources which Saur et al. (2008) estimated would be activated in his model. To show the effects of the strength determination function sources with positive ejection rates are distinguished from dormant jets.

2.3 Conclusion

A penetrator mission to the moon Enceladus is proposed. One of the key challenges in this proposal is targeting the jet sources to reach the subsurface ocean. To solve this problem we present the concept of vectoring in forward flight, where the penetrator is able to thrust laterally during the "free fall" portion of the descent. A control system is needed to steer the spacecraft towards the geyser sources during this phase of the mission. To aid in the development and testing of such a system, a fine-scale model of the Enceladus plume is proposed. This model differs from others in the sense that it focuses on the small scale jets instead of the large, diffused plume. In addition, the ability to create a variety of realistic simulations is crucial to the testing of a system. Although the dynamics of the jets and plume are still not well understood, an algorithm can be tested for robustness to gain confidence in the mission in the face of the unknowns.

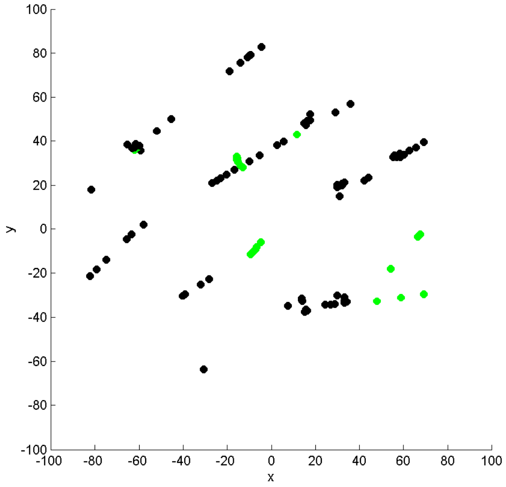

Figure 2.4: **Activation of Jets** The figure shows the results of the random distribution of 100 jet locations on the tiger stripes with 50% corresponding to Spitale and Porco (2007) source locations. Green marks indicate jets that are activated at a true anomaly of 100^o and the black marked jets are those which are not discharging.

Chapter 3

Autonomous Control

3.1 Introduction

The earliest robotic techniques for locating an odor source consisted of only instruments for measuring the concentration of the substance of interest. The most fundamental of these designs is the Braitenberg vehicle (Braitenberg, 1984) which employs two chemical sensors directly connected to each wheel. The level of concentration proportionally drives the motor of the wheel it is connected to and thus the instantaneous chemical gradient controls the vehicle. In turbulent plumes the instantaneous gradient and the direction to the plume source are often not aligned, and therefore more information is needed to efficiently find the source. Most current techniques for robotic scent tracking are aided by a wind sensor, or the equivalent sensor for detecting the forcing function in the relevant fluid. Measurements of the plume can be compared with models of the plume's structure and used to estimate position and model parameters with the Kalman filter (Ishida et al., 1998). With knowledge of the forcing function, information about the plume structure can be inferred, allowing more advanced guidance systems to anticipate where more information can be found as opposed to heading directly for the estimated source location (Vergassola et al., 2007). Source likelihood maps (SLIM) can be achieved with this combination of measurements. Farrell and Pang proposed a method for creating a SLIM based on hidden Marcov methods (HMM) (Farrell et al., 2003) and later improved upon their results by using Bayesian methods (Pang and Farrell, 2006). Kowadlo and Russell (2005, 2006) developed a reactive source localization system based on naive physics which instead of using a SLIM would control the instantaneous heading and velocity of the vehicles.

Plume-tracing is a well observed behavior in nature. Lobsters have been observed to forage based on scent and robotic replication of their behaviors have been implemented (Grasso et al., 2000). Long range olfactory based navigation has been viewed in sea birds (Nevitt, 1999). Many insects have been seen to forage for mates using olfactory methods in response to pheromones including moths (Mafra-Neto and Carde, 1994), wasps (Kerguelen and Card, 1996), and mosquitoes (Zwiebel and Takken, 2004). Moths tracking odor plumes in search for potential mates is currently the most well-document biological scent-tracing behavior, with extensive observations performed by Farkas and Shorey (1972) and Mafra-Neto and Carde (1994) among many. Efforts have been made to robotically replicate search strategies seen in many of these animals.

Here we report on two search strategies and the development on these algorithms to date. The first algorithm is an adaptation of the Kalman filter and Non-Linear Least Squares Algorithms for determining location within a plume, as well as plume parameters to fit model data to measurements. The second method uses a recurrent neural network to capture the behaviors observed in male moths while using scent tracking techniques to find female mates. In both cases, limited success has been realized in simplified testing environments. More development is needed before the controllers can operate in realistic conditions.

3.2 Kalman filtering

The Kalman filter is an optimal state estimation technique for linear observation problems and is commonly used for navigation purposes. For the purpose of plume tracing and tracking methods we define navigation as the simultaneous problem of determining the vehicle position in relationship with the plume source and also with the plume structure. In our case here, that means determining the parameters that define the structure simultaneously as the position of the vehicle. This section will be outlined as such: the next section outlines the model used for concentration levels inside the plume, as well as the parameters needed for filtering purposes; the following section details the use of non-linear least squares, which is an offline version of the extended Kalman filter principle; lastly we show some of the results obtained to date and some conclusions.

3.2.1 Model

The measurement suite on board the rover is assumed to be able to measure the absolute concentration in addition to the gradients as well as the wind vector. The measurement model is given by Equations 3.1 - 3.4.

$$C(x,y) = Q\ exp\left(\frac{-x^2}{uK}\right) exp\left(\frac{-y^2u}{4kx}\right) \tag{3.1}$$

$$\frac{\delta C}{\delta x}(x,y) = \left[\frac{uy^2}{4kx^2} - \frac{2x}{uk}\right] Q\ exp\left(\frac{-x^2}{uK}\right) exp\left(\frac{-y^2u}{4kx}\right) \tag{3.2}$$

$$\frac{\delta C}{\delta y}(x,y) = -\frac{uy}{2kx}\ exp\left(\frac{-x^2}{uK}\right) exp\left(\frac{-y^2u}{4kx}\right) \tag{3.3}$$

$$\theta = \theta \tag{3.4}$$

In this case, Q, u and K are all defined and known. The covariance matrix P is a 3×3 matrix as shown in below.

$$P = \begin{bmatrix} c_x & 0 & 0 \\ 0 & c_y & 0 \\ 0 & 0 & c_\theta \end{bmatrix} \tag{3.5}$$

The Jacobian of the measurement model is needed for the non-linear least squares algorithm. The Jacobian for the measurement model is complex but can be solved directly from the measurement model in Equations 3.1 - 3.4.

$$H = \begin{bmatrix} \frac{\delta C}{\delta x} & \frac{\delta C}{\delta y} & \frac{\delta C}{\delta \theta} \\ \frac{\delta C_x}{\delta x} & \frac{\delta C_x}{\delta y} & \frac{\delta C_x}{\delta \theta} \\ \frac{\delta C_y}{\delta x} & \frac{\delta C_y}{\delta y} & \frac{\delta C_y}{\delta \theta} \\ \frac{\delta \theta}{\delta x} & \frac{\delta \theta}{\delta y} & \frac{\delta \theta}{\delta \theta} \end{bmatrix} = \begin{bmatrix} \left[\frac{uy^2}{4kx^2} - \frac{2x}{uk}\right] C(x,y) & -\frac{uy}{2kx} C(x,y) & 0 \\ \left[\frac{16x^2 - 32ukx^4 - (16ux^3 - 8ku^3x - u^4)y^2}{16k^2u^2x^4}\right] C(x,y) & \left[\frac{uy(1-x)}{2kx^2}\right] C(x,y) & 0 \\ \left[\frac{u^2y^2 + 2u^2y - 8x^3}{4ukx^2}\right] C(x,y) & \left[\frac{-2u(y+1)}{4kx}\right] C(x,y) & 0 \\ 0 & 0 & 1 \end{bmatrix} \tag{3.6}$$

3.2.2 Non-Linear Least Squares

Let us denote our model of the methane concentration as a function $C = f(\mathbf{x}, \mathbf{g}, \nu)$ where the vector $\mathbf{x}$ denotes the states we are wishing to estimate and $\mathbf{g}$ repersentes the knowns in the model, and ν is zero-mean white noise. The goal of this algorithm is given multiple knowns $\mathbf{g}$ and the measured value of the concentration corrosponding to the knowns, we wish to give an estimate of the parameters $\mathbf{x}$ such that the sum of the squares between the actual measurements and the modeled measurements given by f are minimized.

We define the current estimate of the $\mathbf{x}$ as $\tilde{\mathbf{x}}$. If we linearize the function f around $\tilde{\mathbf{x}}$ using a Taylor Series we get.

$$C = f(\tilde{\mathbf{x}}, \mathbf{g}, \nu) + \sum_{\mathbf{j=1}}^{\mathbf{k}} (\partial \mathbf{f} / \partial \mathbf{x_j})(\mathbf{x_j} - \tilde{\mathbf{x}}_\mathbf{j}) \tag{3.7}$$

$$C = f(\tilde{\mathbf{x}}, \mathbf{g}, \nu) + \mathbf{F}(\mathbf{x} - \tilde{\mathbf{x}}) \tag{3.8}$$

Because we are searching for multiple dependent variables, we need an equal or greater number of measurements for our function to be observable. We define the function h as a $N \times 1$ vector which gives the expected measurements for multiple combinations of the known $\mathbf{g}$ given a constant value for the states.

$$h(\hat{\mathbf{x}}, \mathbf{g}, \nu) = [\mathbf{f}(\hat{\mathbf{x}}, \mathbf{g_1}, \nu), \mathbf{f}(\hat{\mathbf{x}}, \mathbf{g_2}, \nu), \ldots, \mathbf{f}(\hat{\mathbf{x}}, \mathbf{g_N}, \nu)]^\mathbf{T} \tag{3.9}$$

The new linearization is:

$$C = h(\tilde{\mathbf{x}}, \mathbf{g}, \nu) + \sum_{\mathbf{i=1}}^{\mathbf{N}} \sum_{\mathbf{j=1}}^{\mathbf{k}} (\partial \mathbf{h_i} / \partial \mathbf{x_j})(\mathbf{x_j} - \tilde{\mathbf{x}}_\mathbf{j}) \tag{3.10}$$

$$C = h(\tilde{\mathbf{x}}, \mathbf{g}, \nu) + \mathbf{H}(\mathbf{x} - \tilde{\mathbf{x}}) \tag{3.11}$$

The innovation is defined as the difference between the measurements and the expected measurements based off the linearized model.

$$\epsilon = y - [h(\tilde{\mathbf{x}}, \mathbf{g}, \nu) + \mathbf{H}(\mathbf{x} - \tilde{\mathbf{x}})] = \delta_\mathbf{y} - \mathbf{H}\delta_\mathbf{x} \tag{3.12}$$

Where δy is the difference between the measurement and the modeled measurement at the centering point of the linearization, and δx is the difference between the state and the centering point of the linearization. The function which we are trying to minimize is the sum of the squares of each term in the innovation.

$$J = \epsilon^T \epsilon = [\delta_y - H\delta_x]^T [\delta_y - H\delta_x] \tag{3.13}$$

$$J = \delta_y^T \delta_y - \delta_x^T H^T \delta_y - \delta_y^T H \delta_x + \delta_x^T H^T H \delta_x \tag{3.14}$$

$$J = \delta_y^T \delta_y - 2\delta_y^T H \delta_x + \delta_x^T H^T H \delta_x \tag{3.15}$$

We want to determine the direction in the state space that must be traveled to minimize J, i.e. the δx vector. We take the first derivative of j with respect to δx and solve for δx.

$$\frac{\partial J}{\partial \delta_x} = -2\delta_y^T H + 2\delta_x^T H^T H = 0 \tag{3.16}$$

$$\delta_x = (H^T H)^{-1} H^T \delta_y \tag{3.17}$$

Now that we have the direction, we normalize the δ_x vector so that we only travel some small amount each step. This prevents us from traveling outside the domain where the linearization is valid.

```
$\hat{\mathbf{x}}$ = initial estimate
repeat
    $\hat{y} = h(\hat{\mathbf{x}}, \mathbf{g})$
    $\delta_y = y - \hat{y}$
    $\delta_x = (H^T H)^{-1} H^T \delta_y$
    $\hat{\mathbf{x}} = \hat{\mathbf{x}} + \frac{\mathbf{t}}{\|\delta_\mathbf{x}\|} \times \delta_\mathbf{x}$
until $\delta_x = 0$ or $\delta_y = 0$
```

3.2.3 Results

The results for the non-linear least square algorithm were inconsistent. A common problem was divergence of the algorithm, and therefore many checks had to be inserted to ensure that the algorithm was working properly and to reset if it wasn't. Another common issue involved the relationship between the position of the source, and the source size. For noisy measurements, the least-squares solution sometimes included a larger source size, and a smaller position vector when in fact the source was small in size and far away. Lastly, the algorithm worked the best when the data points used were spread throughout the plume structure. This is of course problematic as an online rover travels continuously throughout the plume, therefore keeping the data points used at any particular iteration of the algorithm fairly close spatially.

Although the divergence problem can be solved with checks and numerical remedies, the mathematical problem can not be entirely removed. To address the relationship between source size and position, Ishida et al. (1998) created new parameters out of combinations of the model variables and estimated these new parameters with the least squares algorithm. Ultimately, there is more work to be done for this algorithm to be tested on a robotic platform. This section details the localization techniques for determining the position of the vehicle in the plume. Determining the best guidance and control systems to work in tangent with this localization technique is still needed. It may be found that particular patterns of motion work best to give the algorithm the most diverse data points. This may help address the problem seen in the testing.

3.3 Neural Networks for Combined Localization and Control

Artificial neural networks (henceforth referred to simply as neural networks) are mathematical structures which use sequences of nonlinear computations to represent a nonlinear function. The most common structure for a feed-forward neural network is the multilayer perceptron (MLP) which involves an input layer, hidden layer(s), and an output layer. Each hidden layer consists of an arbitrary number of neurons. The input layer consists of the inputs to the system, and the output layer consists of a number of neurons consistent with the number of desired outputs. Between each layer of neurons are connections as shown in Figure 3.1 that propagate the activation of the neuron to all neurons of the next layer. Each of these connections is weighted. The activation of any neuron is given by the sum of all weighted activations from the layer previous put through an activation function. The activation function is usually sigmoid in nature and can be binary (ranging from 0 to 1) or bipolar (ranging from -1 to 1). We use the bipolar sigmoid function. The constant coefficient A can be adjusted to change the gradient of the activation function. It can be set by the user or it can be optimized as part of the training algorithm.

$$g(x) = \frac{2}{1 + \exp(-Ax)} - 1 \tag{3.18}$$

In order for the neural network to successfully represent the desired nonlinear function, the weights in the network are adjusted through a training scheme, of which there are many. The most popular method for training MLP is the backpropagation method which is a gradient decent method. A training set of input-output pairs is used to train the network. The inputs are fed into the network and the activations are fed forward to the output layer. The difference between the given output and the desired output (sometimes called the innovation) is computed and is propagated backwards through the network to adjust the weights between each layer. It has been shown that the backpropagation method is simply a degenerate form of the extended Kalman filter (Ruck et al., 1992) which requires much less computations to achieve the same level of accuracy in training.

Feed-forward networks, including the multilayer perceptron, are well suited for many classification problems where inputs are directly matched to target outputs. These tasks include speech recognition and image processing among others. Feed-forward networks are not suited for tasks where knowledge of previous inputs or outputs influences the current output. In order to take advantage of previous inputs and the corresponding response, feedback is introduced into the structure of the neural network. We refer to networks with this type of structure as recurrent neural networks (RNN). There are many differing structures for recur-

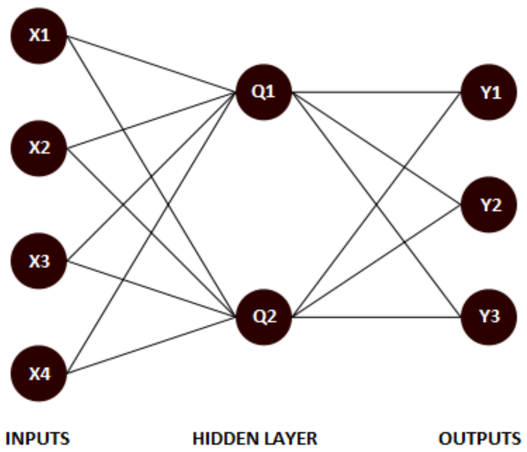

Figure 3.1: **The Multi-Layer Perceptron** This is an example of a MLP with 4 inputs, 1 hidden layer with 2 neurons, and 3 outputs. A weight exists for each connection shown.

rent neural networks, mostly defined by where the feedback is placed in the structure. Internal feedback is when a neuron feeds back to itself and neurons in the same layer whereas external feedback is when the output activations are fed back to the input layer. Of the training rules for RNNs, the most popular are back-propagation-through-time (BPTT) and real-time recurrent learning (RTRL) (Haykin, 2009). The BPTT algorithm involves unfolding the network into a feed-forward network in order to calculate the gradient information while taking into account previous inputs by expanding the network for each term in the pattern.

For this reason, patterns are usually truncated to workable sizes to avoid the large computation and complexity involved with training. RTRL propagates an estimate of the gradient information forward in time, allowing the network to be trained in real time. The RTRL algorithm is also shown to be a degenerate form of the extended Kalman filter. In both the Kalman filter and RTRL methods, calculating the gradients can be complex, especially in networks with many weights. In all the algorithms above, the forced learning technique has been found to improve the stability of training and the training time. Forced learning involves using the desired activations in the feedback process instead of those calculated. This helps by not punishing the network for the feedback of past errors.

3.3.1 Training Scheme

A survey of insects, techniques for plume tracking has been conducted by Murlis et al. (1992). They mostly focus on work done by studying the attraction of male moths to females, and note that there are two distinct phases of plume-tracking: acquiring the plume and following the plume. In the acquisition phase, the moth exhibits a casting pattern, where they move perpendicular to the wind direction back-and-forth, progressively widening their passes until they reconnect with the plume. Once the plume is located the moth heads upwind in bursts until the plume is inevitably lost again, or until the female is located visually. Mafra-Neto and Carde (1994) also did experiments with moths and noticed that the moths did not fly upstream in the plume in all cases. Two types of plumes were used: ribbon plumes characterized as a continuous but meandering plume with low Reynolds number, and a turbulent plume that consisted of odor pulses separated by gaps of lower concentration or clean air. In situations where the ribbon plume was encountered, the moths flew at a slow rate with a zigzag pattern, and would fly upwind and quickly when the turbulent plume was encountered. We will attempt to teach our system behaviors in three stages. The first will be the casting pattern that is used to find the plume. The second will be the zigzag meander that is used to track a ribbon

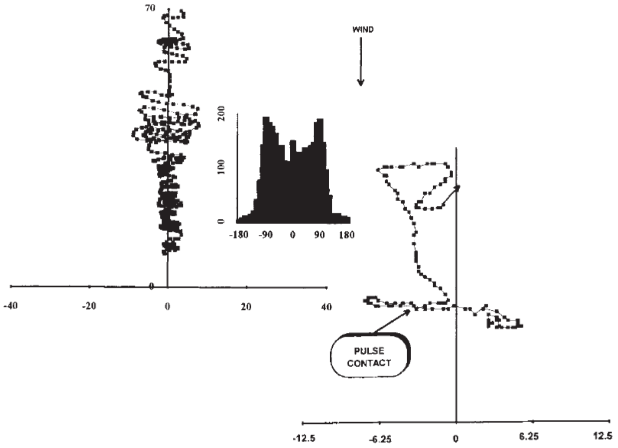

Figure 3.2: **Observed Flight Behaviors in Moths**: Mafra-Neto and Carde (1994) show their results of observing male moths fly through pheromone plumes. Two different plumes are used: ribbon plumes where the moths typically travel slow and zigzagging, and turbulent plumes which moths cast until they location the plume and then quickly move upwind.

plume. Finally we will try to add the ability for the system to know whether it is in a ribbon or turbulent plume, and perform the high-speed, upwind traverses in this situation.

In order to train the network to react to concentration and wind inputs the same way as a moth, we must first develop training patterns. We begin with the ribbon plume case where we wish the network to zigzag through the plume, decreasing the width of the zigzag as it gets closer to the plume source. To get the training sets we take a Gaussian plume (equivalent as used in section 3.2.1) and take cross-wind slices at random locations. We solve the necessary velocity pattern for the vehicle to cast between the 2σ of the max concentration for each slice. We then train the network with the training algorithm describe in the next section. For each iteration of the training scheme, we use a random training set so the network does not over-constrain itself to any one Gaussian slice, but rather generalizes to the 2σ casting pattern.

3.3.2 Training Algorithm

In large neural networks, calculating the gradient information needed to perform either real-time recurrent-learning or extended Kalman filter methods can be extensive. We take advantage of the unscented Kalman filter (UKF) that does not involve explicit computation of the gradients. For the UKF learning rule, we include both the activations of each neuron, and the weights between each layer as the state vector as in Equation 3.19, where x is the state vector, u is a vector of the activations of all neurons, and w is a vector of all the weights in the network.

$$x = \begin{bmatrix} u \\ w \end{bmatrix} \tag{3.19}$$

The UKF uses 2M sigma points, where M is the length of the state vector. These sigma points are defined by Equation 3.20, where P_{xx}^j is the jth row of the covariance matrix for the state vector.

$$\begin{aligned} \sigma_j &= x + (\sqrt{MP_{xx}^j})^T & j &= 1 \dots M \\ \sigma_j &= x - (\sqrt{MP_{xx}^j})^T & j &= M+1 \dots 2M \end{aligned} \tag{3.20}$$

We propagate the inputs through each variation of the network corresponding to the sigma points. The mean of all propagated networks is taken to be the true state at the next time step. The output values are taken to be the mean of all the outputs from the sigma-networks and both the covariance matrix for the outputs and the cross-covariance matrix are calculated for the states and the outputs. The Kalman gain and covariance updates are a relation of the output-covariance and the cross-covariance:

$$K = P_{xy} P_{yy}^{-1} \tag{3.21}$$

$$x^{+} = x^{-} + K(d - \hat{y}) \tag{3.22}$$

$$P_{xx}^{+} = P_{xx}^{-} - K P_{yy} K^{T} \tag{3.23}$$

Where the +’ and ’ denote before and after the innovations update, K’ is the Kalman gain, and d’ is the desired output. Because the activations are included in the state vector, forced learning implicitly takes place when the activations are updated by the innovations process.

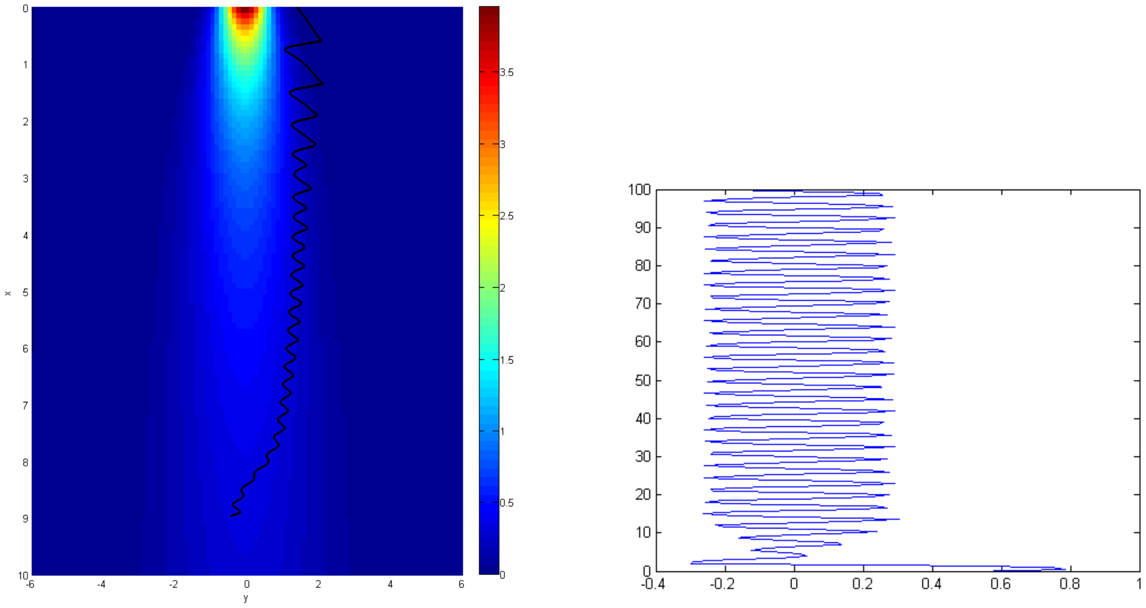

(a) Trajectory of Vehicle COntroled by RNN

(b) Velocity Commands returned by the RNN in response to measured concentrations

Figure 3.3: **RNN Results**; The figures show the results for the recurrent neural network. It is seen that the vehicle cast up the plume, with the width of the casting pattern decreasing as the vehicle gets closer to the source.

3.3.3 Results

The structure of a neural network greatly impacts the complexity of the problems it can solve. It also adds to the difficulty in solving for the optimal weights. Because the number of weights increases exponentially with additional neurons, we try to reduce the structure of the network as much as possible while still achieving the task of casting up towards the source. We began with a simple 1-layer, 2-neuron network with internal feedback. This very simple network was trained until it was able to navigate the odor plume. However, the network was inconsistent and therefore we added another neuron to the network. The new network was trained from the successful weight-function of the previous network by setting all new weights to zero. This was repeated for a 1-layer, 4-neuron network where we saw consistent results. These results can be seen in Figure 3.3.

3.4 Conclusion

Recurrent neural networks emulate the behaviors of scent tracking animals and insects for the purpose of detecting sources of methane on Mars. The neural network has many benefits: it provides a computationally light algorithm for reproducing a desired behavior in response to measurements; neural networks tend to generalize their behavior in situations where they have not been explicitly trained; and once trained they are easy to implement. The downside to using neural networks is the amount of effort required to train them. Both structure and training rules will need to be adapted depending on the results, and additional inputs may be needed for convergence.

The neural networks used have very limited memory capabilities, whereas the source likelihood maps discussed earlier provide more information to the controller on the information gathered over time. In addition, the controller and source identification system are independent. Reactive vs. predictive systems are an important consideration when accounting for obstacle avoidance in addition to source finding. Furthermore, in more advanced systems, additional information other than wind speed and direction and local concentration information may be used. Using the rovers cameras will allow us to rule out certain areas as unlikely sources of methane and may reduce searching time. Passing this information to the neural network to take advantage of it may be more difficult than in traditional likelihood map methods. As stated earlier, the neural network does not face the boundary limitations of the tradition SLIM, however it should be possible to alter these boundaries during the traverse.

Effort will continue in training the networks to perform the tasks required. Should the networks be able to behave as desired in all situations, including navigation control will be required to avoid obstacles. The neural field, which is a completely interconnected recurrent neural network, has been used for navigating obstacles to a target location. It may be found that the neural field can be combined with the currently proposed system to implement both tasks simultaneously.

The Advanced Concepts Team explored a different option for the training of the neural networks, i.e., by using evolutionary algorithms. The potential advantage of this approach over the use of backpropagation discussed above, is that no desired outputs have to be defined. Instead of mimicking a behavior that is optimal for a specific type of animal, this *evolutionary robotics* approach allows to find behaviors that are (approximately) optimal for the specific robot setup. The evolutionary approach has been applied in the past to simplified settings of odor source localization, such as on a pure diffusion scenario Beer and Gallagher (1992); Izquierdo and Buhrmann (2008). However, we believe that it can also be applied to more difficult cases. Figure 3.4 shows a preliminary result of an agent that was evolved for performing odor localization on a stable plume that is transported downwind. The agent starts downwind from the source and uses a feedforward neural network to move toward and circle around the source.

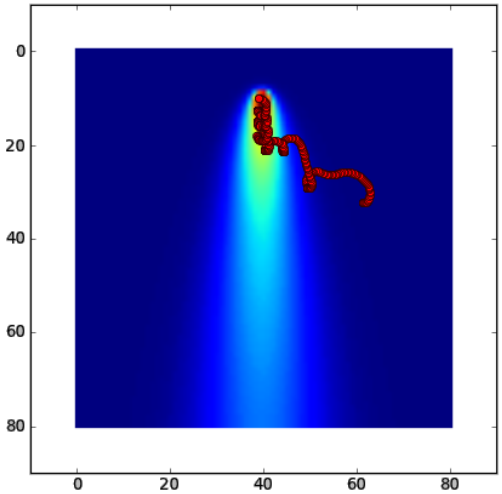

Figure 3.4: Trajectory of a simulated robot (red dot) that is controlled by a feedforward neural network. The neural network has been evolved for finding the odor source in the case of stable plumes as the one in the figure.

Chapter 4

Conclusions

This report details the work done on the Ariadna Study: Scent for Science performed by Carleton University in partnership with the European Space Agency's Advanced Concepts Team. The scent for science methodology attempts to gather scientific information in similar ways as insects and other animals track and trace odor plumes to their source. Two scenarios where the scent for science methodology made sense were the search for sources of Martian methane with a planetary rover vehicle, and targeting Enceladus' icy jets with the use of a planetary penetrator for subsurface exploration science. Models of each scenario environment were developed and tested, and preliminary work on control techniques for plume tracing and scent tracking were explored.

The Martian methane plume model varied from previous Martian models due to the fact that the spatial scale was considerably lower. Measurements of the methane had resolution on the order of kilometers and tens of kilometers. The simulation for our model was 100 meters by 100 meters which is more realistic of what a Mars rover would travel. Partial differential equations were solved to model the flow of methane throughout the simulated area. A wind model with three different spatial scales was used to achieve the desired plume affects. An analysis of the plume was conducted and compared to experimental results and a previous plume models for representing moth pheromones. The numerical statistics show that the model has the characteristics which makes plume tracking non-trivial.

Models of Enceladus' plume focus on the large scale dynamics of the plume as to compare the model with measurements of the Cassini spacecraft. For a high-speed descent mission, the structure of the individual jets is just as important as the diffusion of these jets into the plume structure. We therefore create a new model which includes many more jets than the eight traditional used to represent the sources located by Spitale and Porco (2007). Due to the short time scale of a penetrator mission in relationship to the dynamics of the plume, we create a static model. To add variability to the model for testing the robustness of algorithms developed jet locations are assigned randomly, yet realistically. Tidal stress models are included in order to determine the emission rate for jets throughout the tiger stripes for a specified orbital position of the moon. This allows for even more testing, and the beginning of mission planning. Results are compared to other models to ensure similar trends are followed, but exact numerical values are not constrained as the plume and jet dynamics are still fairly unknown.

Preliminary work was done in the control and localization problem. Two techniques were explored: the use of the Kalman filter to identify the position of the rover in the plume by comparing measurements to a model, and the use of a recurrent neural network to encode the behaviors observed in male moths attempting to find female mates through the use of tracking pheromones. Limited success was achieved in both strategies for static, simple odor plumes. More development is needed before either technique will be able to navigate the complex turbulent plumes of the Mars methane model. Finally, at the Advanced Concepts Team another, evolutionary robotics approach was followed to autonomous odor source localization. Preliminary experiments show that feedforward neural networks can localize a source in an environment with a stable plume. Future work should show whether the approach generalizes to more turbulent scenarios.

Future work on the Martian methane model will include a study on the difference between terrestial and

Martian winds to determine what (if any) subtle difference might be desired in the statistical values. In addition, the computational cost of running the Martian methane model is fairly high. If many scenarios need to be continuously generated, it may be worthwhile to evaluate the computation and attempt to lower it. Additional work on the Enceladus model would be to update the stress model as more information about the relationship between the plume and the tidal stresses become available. Updates may need to be made to both the values of the normal and shear stress over the orbital period, as well as the emission rates of the jets in response to those stresses. Of course, constant development in the control and navigational algorithms will continue to improve effectiveness.

Bibliography

V. Braitenberg. *Vehicles: Experiments in Synthetic Psychology.* The MIT Press, Boston, MA, 1984.

Eric Chassefière. Metastable methane clathrate particles as a source of methane to the martian atmosphere. *Icarus*, 204(1):137–144, November 2009.

Brendon K. Chastain and Vincent Chevrier. Methane clathrate hydrates as a potential source for martian atmospheric methane. *Planetary and Space Science*, 55(10):1246–1256, July 2007.

P.C. Chatwin. The use of statistics in describing and predicting the effects of dispersing gas clouds. *Journal of Hazardous Materials*, 6:213–230, 1982.

C Chyba and C Phillips. Possible ecosystems and the search for life on Europa. *Proceedings of the National Academy of Sciences of the United States of America*, 98(3):801–4, 2001.

Y. Dong, T. W. Hill, B. D. Teolis, B. a. Magee, and J. H. Waite. The water vapor plumes of Enceladus. *Journal of Geophysical Research*, 116(A10):1–13, 2011.

S.R. Farkas and H.H. Shorey. Chemical Trail-Following by Flying Insects: A Mechanism for Orientation to a Distant Odor Source. *Science*, 178(4056):67–68, 1972.

J A Farrell, Shuo Pang, and Wei Li. Plume mapping via hidden Markov methods. *IEEE transactions on systems, man, and cybernetics. Part B, Cybernetics : a publication of the IEEE Systems, Man, and Cybernetics Society*, 33(6):850–63, January 2003.

Jay A Farrell, John Murlis, Xuezhu Long, Wei Li, and T Ring. Filament-Based Atmospheric Dispersion Model to Achieve Short Time-Scale Structure of Odor Plumes. *Enviromental Fluid Mechanics*, 2:143–169, 2002.

W. M. Farrell, G. T. Delory, and S. K. Atreya. Martian dust storms as a possible sink of atmospheric methane. *Geophysical Research Letters*, 33(21):2–5, November 2006.

B. L. Fleshman, P. a. Delamere, and F. Bagenal. Modeling the Enceladus plumeplasma interaction. *Geophysical Research Letters*, 37(3):1–5, 2010.

Vittorio Formisano, Sushil Atreya, Thérèse Encrenaz, Nikolai Ignatiev, and Marco Giuranna. Detection of methane in the atmosphere of Mars. *Science (New York, N.Y.)*, 306(5702):1758–61, December 2004.

Frank W Grasso, Thomas R Consi, David C Mountain, and Jelle Atema. Biomimetic robot lobster performs chemo-orientation in turbulence using a pair of spatially separated sensors: Progress and challenges. *Robotics and Autonomous Systems*, 30(1-2):115–131, January 2000.

Richard Greenberg, Paul Geissler, B. Randall Tufts, and Gregory V. Hoppa. Habitability of Europa's crust: The role of tidal-tetonics processes. *Journal of Geophysical Research*, 105(E7):17551 – 17562, 2000.

Candice J Hansen, L Esposito, a I F Stewart, J Colwell, A Hendrix, W Pryor, D Shemansky, and R West. Enceladus' water vapor plume. *Science (New York, N.Y.)*, 311(5766):1422–5, March 2006.

Simon Haykin. *Neural Networks and Learning Machines.* Pearson Education Inc., Saddle River, New Jersey, 2009.

Gregory Hoppa, B Randall Tufts, Richard Greenberg, and Paul Geissler. Strike Slip Faults on Europa : Global Shear Patterns Driven by Tidal Stress. *Icarus*, 141:287–298, 1999.

T.a. Hurford, B.G. Bills, P. Helfenstein, R. Greenberg, G.V. Hoppa, and D.P. Hamilton. Geological implications of a physical libration on Enceladus. *Icarus*, 203(2):541–552, 2009.

Hiroshi Ishida, Takamichi Nakamoto, and Toyosaka Moriizumi. Remote sensing of gas/odor source location and concentration distribution using mobile system. *Sensors and Actuators: B. Chemical*, 49:52–57, 1998.

Y.-D. Jia, C. T. Russell, K. K. Khurana, Y. J. Ma, D. Najib, and T. I. Gombosi. Interaction of Saturn's magnetosphere and its moons: 2. Shape of the Enceladus plume. *Journal of Geophysical Research*, 115 (A4):1–11, 2010.

C D Jones. On the Structure of Instantaneous Plumes in the Atmosphere. *Journal of Hazardous Materials*, 7:87–112, 1983.

S Jurac. Saturn's E Ring and Production of the Neutral Torus. *Icarus*, 149(2):384–396, 2001.

V I Kerguelen and R T Card. Reinforcement Mechanisms of Olfactory Conditioning During Parasitization by the Parasitoid Brachymeria intermedia (Hymenoptera : Chalcididae). *Journal of Insect Behavior*, 9 (6):947–960, 1996.

G. Kowadlo and R. a. Russell. Using naïve physics for odor localization in a cluttered indoor environment. *Autonomous Robots*, 20(3):215–230, June 2006.

Gideon Kowadlo and R Andrew Russell. Improving the robustness of Naive Physics airflow mapping , using Bayesian reasoning on a multiple hypothesis tree . Technical report, 2005.

Vladimir a. Krasnopolsky, Jean Pierre Maillard, and Tobias C. Owen. Detection of methane in the martian atmosphere: evidence for life? *Icarus*, 172(2):537–547, December 2004.

H. Kriegel, S. Simon, J. Müller, U. Motschmann, J. Saur, K.-H. Glassmeier, and M.K. Dougherty. The plasma interaction of Enceladus: 3D hybrid simulations and comparison with Cassini MAG data. *Planetary and Space Science*, 57(14-15):2113–2122, 2009.

Franck Lefèvre and François Forget. Observed variations of methane on Mars unexplained by known atmospheric chemistry and physics. *Nature*, 460(7256):720–3, August 2009.

John L. Lumley and Hans A. Panofsky. *The structure of atmospheric turbulence.* Interscience Publishers, New York, 1964.

Agenor Mafra-Neto and Ring Carde. Fine-scale structure of phermone plumes modulates upwind orientation of flying moths. *Nature*, 369:142–144, 1994.

Michael a. Mischna, Mark Allen, Mark I. Richardson, Claire E. Newman, and Anthony D. Toigo. Atmospheric modeling of Mars methane surface releases. *Planetary and Space Science*, 59(2-3):227–237, February 2011.

Micheal Mumma, Geronimo Villanueva, Robert Novak, Tilak Hewagama, Boncho Bonev, Micheal DiSanti, Avi Mandell, and Micheal Smith. Strong Release of Methane on Mars in Northern Summer 2003. *Science*, 323(February):1041–1045, 2009.

John Murlis, Joeseph Elkinton, and Ring Carde. Odor plumes and how insects use them. *Anni. Rev. Entomol.*, 37(86):505–532, 1992.

G Nevitt. Olfactory foraging in Antarctic seabirds:a species-specific attraction to krill odors. *Marine Ecology Progress Series*, 177:235–241, 1999.

F Nimmo, J R Spencer, R T Pappalardo, and M E Mullen. Shear heating as the origin of the plumes and heat flux on Enceladus. *Nature*, 447(7142):289–91, 2007.

K S Olsen and K Strong. Small-scale methane dispersion modelling for possible plume sources on the surface of Mars. 2012.

Shuo Pang and Jay a Farrell. Chemical plume source localization. *IEEE transactions on systems, man, and cybernetics. Part B, Cybernetics : a publication of the IEEE Systems, Man, and Cybernetics Society*, 36 (5):1068–80, October 2006.

Christopher D Parkinson, Mao-Chang Liang, Yuk L Yung, and Joseph L Kirschivnk. Habitability of enceladus: planetary conditions for life. *Origins of life and evolution of the biosphere : the journal of the International Society for the Study of the Origin of Life*, 38:355–69, 2008.

C C Porco, P Helfenstein, P C Thomas, a P Ingersoll, J Wisdom, R West, G Neukum, T Denk, R Wagner, T Roatsch, S Kieffer, E Turtle, a McEwen, T V Johnson, J Rathbun, J Veverka, D Wilson, J Perry, J Spitale, a Brahic, J a Burns, a D Delgenio, L Dones, C D Murray, and S Squyres. Cassini observes the active south pole of Enceladus. *Science (New York, N.Y.)*, 311(5766):1393–401, 2006.

F Postberg, S Kempf, J Schmidt, N Brilliantov, a Beinsen, B Abel, U Buck, and R Srama. Sodium salts in E-ring ice grains from an ocean below the surface of Enceladus. *Nature*, 459(7250):1098–101, 2009.

Ray T. Reynolds, Steven W. Squyres, David S. Colburn, and Christopher P. McKay. On the habitability of Europa. *Icarus*, 56(2):246–254, 1983.

Dennis Ruck, Steven Rogers, Matthew Kabrisky, Peter Maybeck, and Mark Oxley. Comparative Analysis of Backpropagation and the Extended Kalman Filter for Training Multilayer Preceptrons. *IEEE Transactions on Pattern Analysis and Machine Intelligence*, 14(6):686–691, 1992.

Joachim Saur, Nico Schilling, Fritz M. Neubauer, Darrell F. Strobel, Sven Simon, Michele K. Dougherty, Christopher T. Russell, and Robert T. Pappalardo. Evidence for temporal variability of Enceladus' gas jets: Modeling of Cassini observations. *Geophysical Research Letters*, 35(20):1–5, 2008.

J. R. Spencer, J. C. Pearl, M. Segura, F. M. Flasar, A. Mamoutkine, P. Romani, B. J. Buratti, A. R. Hendrix, L. J. Spilker, and R. M. C. Lopes. Cassini Encounters Enceladus: Background and the Discovery of a South Polar Hot Spot. *Science*, 311(March):1401–1405, 2006.

Joseph N Spitale and Carolyn C Porco. Association of the jets of Enceladus with the warmest regions on its south-polar fractures. *Nature*, 449(7163):695–7, 2007.

O.G. Sutton. *Micrometeorology.* McGrw-Hill, New York, 1953.

V. Tenishev, M. R. Combi, B. D. Teolis, and J. H. Waite. An approach to numerical simulation of the gas distribution in the atmosphere of Enceladus. *Journal of Geophysical Research*, 115:1–8, 2010.

F Tian, a Stewart, O Toon, K Larsen, and L Esposito. Monte Carlo simulations of the water vapor plumes on Enceladus. *Icarus*, 188(1):154–161, 2007.

G Tobie, O Cadek, and C Sotin. Solid tidal friction above a liquid water reservoir as the origin of the south pole hotspot on Enceladus. *Icarus*, 196(2):642–652, 2008.

Massimo Vergassola, Emmanuel Villermaux, and Boris I Shraiman. 'Infotaxis' as a strategy for searching without gradients. *Nature*, 445(7126):406–409, January 2007.

John Wahr, Zane a. Selvans, McCall E. Mullen, Amy C. Barr, Geoffrey C. Collins, Michelle M. Selvans, and Robert T. Pappalardo. Modeling stresses on satellites due to nonsynchronous rotation and orbital eccentricity using gravitational potential theory. *Icarus*, 200(1):188–206, 2009.

J Hunter Waite, Michael R Combi, Wing-Huen Ip, Thomas E Cravens, Ralph L McNutt, Wayne Kasprzak, Roger Yelle, Janet Luhmann, Hasso Niemann, David Gell, Brian Magee, Greg Fletcher, Jonathan Lunine, and Wei-Ling Tseng. Cassini ion and neutral mass spectrometer: Enceladus plume composition and structure. *Science (New York, N.Y.)*, 311(5766):1419–22, 2006.

Christopher R. Webster and Paul R. Mahaffy. Determining the local abundance of Martian methane and its 13C/12C and D/H isotopic ratios for comparison with related gas and soil analysis on the 2011 Mars Science Laboratory (MSL) mission. *Planetary and Space Science*, 59(2-3):271–283, February 2011.

Kevin Zahnle, Richard S. Freedman, and David C. Catling. Is there methane on Mars? *Icarus*, 212(2): 493–503, April 2011.

L J Zwiebel and W Takken. Olfactory regulation of mosquito-host interactions. *Insect biochemistry and molecular biology*, 34(7):645–52, July 2004.

E.J. Izquierdo and T. Buhrmann Analysis of a dynamical recurrent neural network evolved for two qualitatively different tasks: Walking and chemotaxis *11th International Conference on Artificial Life*, 257–264, 2008.

R.D. Beer and J.C. Gallagher Evolving Dynamical Neural Networks for Adaptive Behavior *Adaptive Behavior*, 1:1, 91–122, 1992